AJS American Journal of Science
publishing earth-sciences research since 1818

Bryndzia, L. T. (2026). From Source Rock to Cinnabar – How the Giant Mercury Deposits in Earth's Crust Formed. *American Journal of Science*, *326*, Article 2.
https://doi.org/10.2475/001c.147533

Science Paper

From Source Rock to Cinnabar – How the Giant Mercury Deposits in Earth's Crust Formed

L. Taras Bryndzia[1][a]

[1] Principal - LTB Consulting Services LLC

Keywords: Mercury, cinnabar, Hg isotopes, LIP sediments, source rocks, redox state

https://doi.org/10.2475/001c.147533

American Journal of Science

Vol. 326, 2026

The largest concentrations of Hg on Earth exist as giant deposits of cinnabar (HgS). How such enrichments of Hg formed, based on its known crustal abundance has never been fully resolved, nor has the source(s) of Hg been unequivocally established. Hg isotopes were used to elucidate crustal processes leading to the concentration of Hg during thermal maturation of Hg and organic matter enriched sediments and cinnabar formation. Mass dependent fractionation (MDF) of Hg isotopes shows remarkable enrichment of ^{202}Hg in cinnabar relative to its upper mantle source. Two mechanisms contribute to this enrichment: one is the low temperature, early diagenetic loss of volatile $^{198}Hg^0_{(g)}$ to an extant gas phase; the other is oxidation during cinnabar deposition. Loss of $^{198}Hg^0_{(g)}$ results in ^{202}Hg enrichment of Hg in residual organic matter in source sediments. Evidence for this significant loss of $^{198}Hg^0_{(g)}$ is observed as large depletions in the $\delta^{202}Hg$ isotopic composition of proximal gas condensate liquids in high pressure – high temperature (HP/HT) reservoirs in the central North Sea (CNS). Migration of hydrocarbons and formation brines from Hg-enriched sediments transports reduced $Hg^0_{(org,\ aq)}$ to the site of cinnabar deposition, where oxidation of $Hg^0_{(org,\ aq)}$ and H_2S further enhances enrichment of ^{202}Hg in cinnabar. The large changes in MDF are independent of mass independent fractionation (MIF) of mercury isotopes.

Approximately 80% of the cinnabar samples examined in this study plot within ± 0.1‰ of the origin on a $\Delta^{199}Hg$ - $\Delta^{201}Hg$ MIF Hg isotope plot and have a Hg isotopic composition similar to that of continental flood basalts (CFB), consistent with an upper mantle source for Hg. MIF trends defined by coals and euxinic sediments on $\Delta^{199}Hg$ - $\Delta^{201}Hg$ MIF plots have $\Delta^{199}Hg$ /$\Delta^{201}Hg$ slopes ~1. These tend to be the most reduced Hg-enriched sediments, deposited in anoxic or euxinic environments in which the dominant Hg species is Hg^0. In open marine environments the dominant Hg species is likely to be Hg^{2+}. $\Delta^{199}Hg$ /$\Delta^{201}Hg$ slopes >1 deviating from these reduced sediment trends appear to be controlled by the fugacity of H_2S (fH_2S), and variable proportions of reduced Hg^0 to oxidized Hg^{2+} in progenitor sediments, reflecting their environments of deposition and redox state.

1. INTRODUCTION

Recent research has demonstrated the utility of using Hg anomalies in crustal sediments as proxies for volcanic activity associated with large igneous province (LIP) events, and as proxies for the major extinction events such as those at the Permian–Triassic (PTB) and Cretaceous–Paleogene (K/Pg) boundaries (Bergquist, 2017; Grasby et al., 2017, 2019; Percival et al., 2021; Sial et al., 2016, 2020; Thibodeau et al., 2016). Many Hg anomalies are also closely associated with the timing of globally elevated levels of atmospheric CO_2 that resulted in environmental conditions favorable for the generation and preservation of algal and planktonic blooms, resulting in regions of anoxia in the global oceans (Jenkyns, 2010; Jones et al., 2019; Schlanger & Jenkyns, 1976). Such reducing conditions were favorable for the preservation of organic matter in the geologic record and it is these episodes in Earth history that gave rise to some of the most prolific organic-rich hydrocarbon source rocks on the planet (Bergman et al., 2021). These organic-rich source rocks formed in marine and terrestrial environments in which both organic matter and Hg were preserved (Jenkyns, 2010; Schlanger & Jenkyns, 1976; Yao et al., 2022).

a Corresponding author: ltbryndzia@gmail.com

Numerous attempts have been made to correlate formation ages for many of the most important organic-rich source rock forming events with the timing of LIPs e.g., Sial et al. (2016, 2020); Grasby et al. (2019), and Bergman et al. (2021). The correlations provide strong evidence for the LIP events initiating globally significant source rock deposition. However, the relationship between the timing of many of the LIP events with specific extinction events is less clear, and continues to be the topic of ongoing research e.g., Sial et al. (2020).

Cinnabar (HgS), is the dominant ore mineral of Hg in Earth's crust. Mercury isotopes provide compelling evidence for a genetic association of Hg in cinnabar deposits being sourced from sediments deposited during global LIP events. HgS deposits in the Terlingua mining district of SW Texas, and the New Idria Hg mine in the California Coast Range are examples of Hg recycling from organic-rich marls and tuffaceous black shales of Cenomanian–Turonian age (~94.1 Ma; Eldrett et al., 2015), having a Hg isotopic signature confirming a genetic relationship to the OAE-2 LIP event. It was also shown that Hg isotopes in cinnabar ores were enriched in ^{202}Hg, consistent with the δ^{202}Hg isotopic composition of their sediment source (Bryndzia, 2023; fig. 1).

Hydrocarbons play a vital role in the formation of cinnabar ores, with hydrocarbon liquids being the principal ore-forming fluid that transports Hg as $Hg^0_{(org)}$ from reduced, organic-rich source rocks and Hg-enriched sediments to the site of mineral deposition. As a generalization, it is the oxidation of reduced Hg^0- and H_2S-bearing ore-forming fluids that results in cinnabar deposition (Bryndzia, 2023; Bryndzia et al., 2023; Krupp, 1988).

All of the major cinnabar deposits in table 1 are intimately associated with organic-rich rocks, including carbonaceous black shales, limestone/marls, and claystones (the latter derived from altered tuffaceous material), and both liquid and solid hydrocarbons. Many of the claystones are also significantly enriched in Hg, beyond normal crustal abundances (~62.4 ppb; Grasby et al., 2019). They all preserve evidence for being hydrothermally modified during the cinnabar ore-forming process, mostly driven by heat from proximal volcanic and/or igneous activity. It is appropriate, therefore, to discuss the Hg isotope systematics of hydrocarbons, source rocks and Hg-rich sediments in order to better understand how the largest deposits of cinnabar on Earth formed.

The hypothesis being developed in this paper is that most of the Hg in the world's largest deposits of cinnabar (HgS) was derived from an upper mantle source, similar in Hg isotopic composition to that of CFBs (Yin et al., 2022), and then subsequently remobilized from organic rich source rock sediments by expelled hydrocarbon and reduced formation brines. Mantle derived Hg^0 is ejected with volcanic ash into the Earth's atmosphere, where it undergoes rapid oxidation of $Hg^0_{(g)}$ to Hg^{2+}. Much of this oxidized Hg^{2+} is bound in sediments, both marine and terrestrial, as an alteration product of the very fine-grained ash material. An excellent example of this are the tephra deposits from the Grane oil field in the North Sea, closely associated with claystones and shales throughout the North Atlantic Igneous Province (NAIP). Some of the tuff layers are significantly enriched in Hg, containing up to 17,400 ppb Hg, attributed by Jones et al. (2019) to their close proximity to the source of volcanism.

This paper includes new data on hydrocarbons and source rocks, integrated with previously published Hg isotope data from Hg-enriched sediments, many of which appear to be chronostratigraphically associated with LIPs, and some of the largest Hg ore deposits on Earth (table 1). Mercury isotopes are used to elucidate the processes involving Hg and its subsequent concentration and isotopic enrichment in ^{202}Hg during thermal maturation of organic matter in source rocks and Hg-enriched sediments, and ultimately in cinnabar ores. MDF and MIF fractionation for Hg isotopes is also discussed, together with Hg isotope data for the cinnabar deposits shown in table 1.

2. MATERIALS AND METHODS

2.1. Cinnabar deposits

The Hg ore deposits in table 1 range in age from Cambrian to Miocene, and are hosted in a diverse suite of sediments and sedimentary rocks that include organic-rich claystone and alkaline lake sediments in the Miocene-age McDermitt caldera in Nevada (USA), Lower Cretaceous limestones, shales and marls (SW Texas and Peru), altered serpentinite, sandstone and shale (New Idria, CA Coast Range), sandstones, dolomite, and carbonaceous black shale (Permian–Triassic in Indrija, Slovenia), quartzite (Silurian–Devonian in Almaden, Spain), Cambrian-age carbonaceous black shales in Wanshan and Paiting (SW China), and in marls, limestones, calcarenites and sandstones in Monte Amiata (Tuscany, Italy). Hg isotope data for each deposit were compiled from previously published studies, and together with a short summary of the geological setting are given in supplementary tables S2–S8.

2.2. Source rocks and hydrocarbons

Mercury isotope data for source rocks and hydrocarbons consist of previously unpublished Hg isotope data from the Heather, Pentland, and Kimmeridge shales in the CNS graben, including gas condensate liquids from the CNS, North West Shelf of Australia (NWS), Philippines, and three oil samples from the Eastern Gulf of Mexico (EGOM) in the USA. Mercury isotope data for subsurface formations from the CNS are summarized in table S9, for hydrocarbons in table S10, and source rocks and hydrocarbons from Bohai Bay and Sichuan Basin in table S11, respectively. Mercury isotope data for Hg-enriched sediments are summarized in tables S12–S15 and include the following: OAE-2 sediments from the type locality in Rehkogelgraben (table S12), Cambrian black shales from Maoshi, Zhijin, and Paiting (table S13), PTB sediments (table S14), and LPE sediments (table S15), respectively.

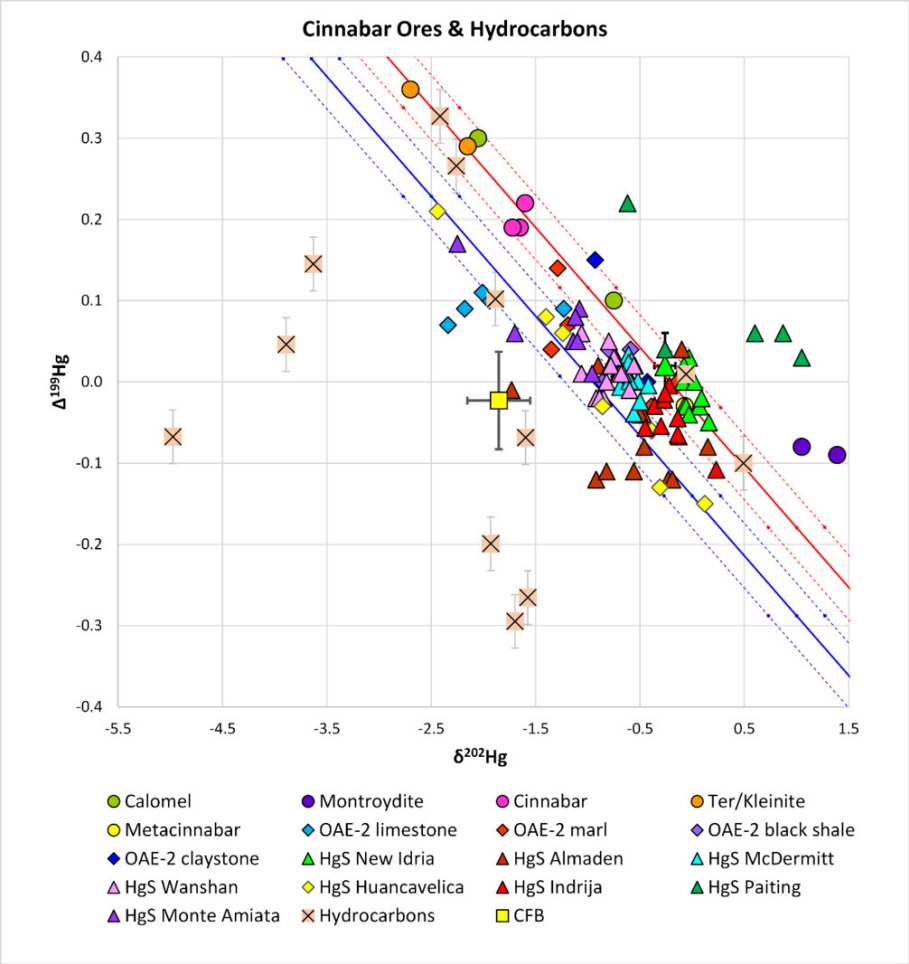

Figure 1. Mercury isotope data for cinnabar deposits in table 1. Also plotted are Hg isotope data from OAE-2 rocks, including limestone, marl, black shale and claystone from Rehkogelgraben, Austria (Yao et al., 2022). Solid red and blue lines are linear best fits to Hg ore minerals from Terlingua and Huancavelica, respectively. Solid round symbols represent a suite of Hg minerals from Terlingua. Dashed red and blue lines represent ± 2σ analytical uncertainty in δ^{202}Hg (Stetson et al., 2009). CFB refers to the Hg isotopic composition of continental flood basalts (Yin et al., 2022). Also plotted are Hg isotopic compositions of a suite of hydrocarbons (table S11; ±2σ). Figure has been modified from Bryndzia (2023).

2.3. Laboratory analyses

All of the Hg isotope data in tables S9 and S11 were measured at ALS Scandinavia AB, (Lulea, Sweden), a commercial laboratory that provides Hg isotope analyses. Details concerning sample preparation, instrumentation and analysis are provided in a separate section on mercury isotopes in the Data and Supporting Information section. Hg isotopes for the three EGOM oil samples in table S10 were analyzed at the University of Michigan Hg isotope laboratory.

3. RESULTS

3.1. Mass dependent fractionation of Hg isotopes

3.1.1. Cinnabar deposits

Mercury isotope data from Terlingua ore minerals, OAE-2 sediments, Huancavelica (Peru), McDermitt (Nevada, USA), Indrija (Slovenia), Almaden (Spain), Wanshan and Paiting (SW China), and Monte Amiata (Tuscany, Italy) are shown in figure 1. Mercury-bearing ore minerals from the Terlingua and Huancavelica deposits display large ranges in MDF (δ^{202}Hg = −3 to 0‰), and an equally large range in MIF, with Δ^{199}Hg ranging from −0.1 to almost 0.4‰. Of all the deposits in table 1, cinnabar ores from Paiting are the most enriched in ^{202}Hg. With this exception, cinnabar from all of the other major Hg deposits in table 1, regardless of host rock age, have a very tight distribution for both MDF and MIF Hg isotope fractionation, ranging from δ^{202}Hg = ~0 to −1‰, and Δ^{199}Hg = 0 ± 0.1‰. Values of δ^{202}Hg for cinnabar from New Idria in the California Coast Range are consistent with the same linear isotope trends as observed for Terlingua, and the Hg isotopic composition for a suite of OAE-2 rocks from the chrono-stratigraphically equivalent type section in Rehkogelgraben, Austria (Bryndzia, 2023; Yao et al., 2022). There are no published Hg isotopic data for associated sediments from the Texas, Peruvian or Tuscany deposits.

Table 1. Major mercury deposits included in this study

Deposit	Location	Host rocks	Age	Hg^0 produced (tonnes)	LIP-OAE / Source Rock Bergman et al. (2021)
Wanshan/ Paiting	East Guizhou, China	Dolostones/black shale	Middle Cambrian	22,000	SPICE?
Almaden	Spain	Sandstone/black shale	Ordovician/Silurian Permian/Triassic	276,000	Sil-Dev boundary Siberian Traps LIP
Idrija	Slovenia	Carboniferous shale Sandstone/dolostone	Carboniferous Permian/Triassic	145,000	Siberian Traps LIP
Monte Amiata	Tuscany, Italy	Limestone/marls/alt tuffs, calcarenites, sandstone	Volcanism/ hydrothermal overprint at ~0.3 Ma	100,000	LIP unknown OAE-2; MCE?
Huancavelica	Peru	Arenite/limestone Intercalated marls, limestone and shale	Lower Cret/Aptian Mineralization age >7 Ma and < 16.9 Ma	51,750	LIP unknown OAE-2; MCE?
Terlingua	SW Texas, USA	Limestone/marls/alt tuffs, black shale	Lower Cretaceous Cenomanian-Turonian	5,175	OAE-2; MCE
New Idria	California, USA	Altered serpentinite, sandstone and shale	Lower Cretaceous Cenomanian-Turonian	17,386	OAE-2; MCE
McDermitt	Nevada, USA	Alkaline lake sediments, altered tuffs, black shale, claystone	Miocene	10,000	Columbia River Plateau/ Monterey

The range of Δ^{199}Hg observed in the cinnabar ore for Hg deposits in table 1 closely matches that of an upper mantle source, represented by continental flood basalts (CFB; Yin et al., 2022). It should be noted that cinnabar ores in all of these Hg deposits are enriched in ^{202}Hg relative to the average mantle Hg isotopic composition. One sample of Almaden cinnabar ore actually plots on the mantle isotopic composition.

The study by Palero-Fernández et al. (2015) addressed the question of timing for Hg ore formation in the Almaden district using Pb-Pb isotope age-dating techniques. Many of the samples analyzed by Palero-Fernández et al. (2015) were also analyzed for their Hg isotopic compositions by Gray et al. (2013). The Pb-Pb ages and Hg isotopic data for Almaden cinnabar data are summarized in table S7 and figure S1. Despite being hosted in the lower Silurian–early Devonian age Criadero Quartzite, only two of eleven cinnabar samples have corresponding host rock ages. Most of the Almaden cinnabar ores have Pb-Pb ages that are either Permian–Triassic or Jurassic–early Cretaceous in age. One sample has an unusually young Oligocene Pb-Pb age. Based on their disparate Pb isotope age data Palero-Fernández et al. (2015) went to great lengths to explain the source of Pb and the very broad range of ages for this giant Hg deposit. However, there is almost no discussion concerning the source(s) of Hg in the Almaden cinnabar ores.

3.1.2. Source rocks

Figure 2 shows a δ^{202}Hg versus Δ^{199}Hg plot of Hg isotope data for a suite of source rocks and hydrocarbons from China, the CNS, NWS, EGOM, and the Philippines. Mercury data for source rocks and hydrocarbons are summarized in table S9, table S10, and table S11, respectively. The Hg concentrations reported in table S11 are for source rocks from China studied by Zhou et al. (2023), and are averages of samples for which Hg isotopes were measured. The range of Hg concentrations in the Bohai Bay terrestrial source rocks are generally low, averaging ~27 ± 15 ppb (n=38; ± 1σ) in Paleogene terrestrial source rocks. Upper Permian marine source rocks contain a very low concentration of Hg, averaging ~5 ± 4 ppb (n=4; ± 1σ), while Lower Triassic marine source rocks contained the highest Hg concentration, averaging ~60 ± 75 ppb (n=4; ±1σ).

Concentrations of Hg for CNS source rocks are quite variable, and range from ~18 ppb in Pentland shale, and ~46 ppb in the deep Kimmeridge and Heather shales, respectively (table S8). On average, these values are similar to the concentration range observed in source rocks from the Sichuan Basin and Bohai Bay by Zhou et al. (2023). By contrast, both the shallow Kimmeridge shale and Pentland coal are much more enriched in Hg, with the Pentland coal samples containing concentrations of 281 and 374 ppb Hg, while the shallow Kimmeridge shale samples contain 242 and 235 ppb Hg, respectively (table S8). The Hg enriched CNS source rocks have Hg concentrations consistent with those reported by Grasby et al. (2019; their fig. 2), for key extinction boundaries and oceanic anoxic events through geologic time.

The black rectangle in figure 2 outlines the area of clastic source rocks (this study; excluding Pentland coals) that include Paleogene-age terrestrial source rocks from Bohai Bay (BB, China), and both marine and terrestrial source rocks ranging in age from early to late Jurassic (CNS) to

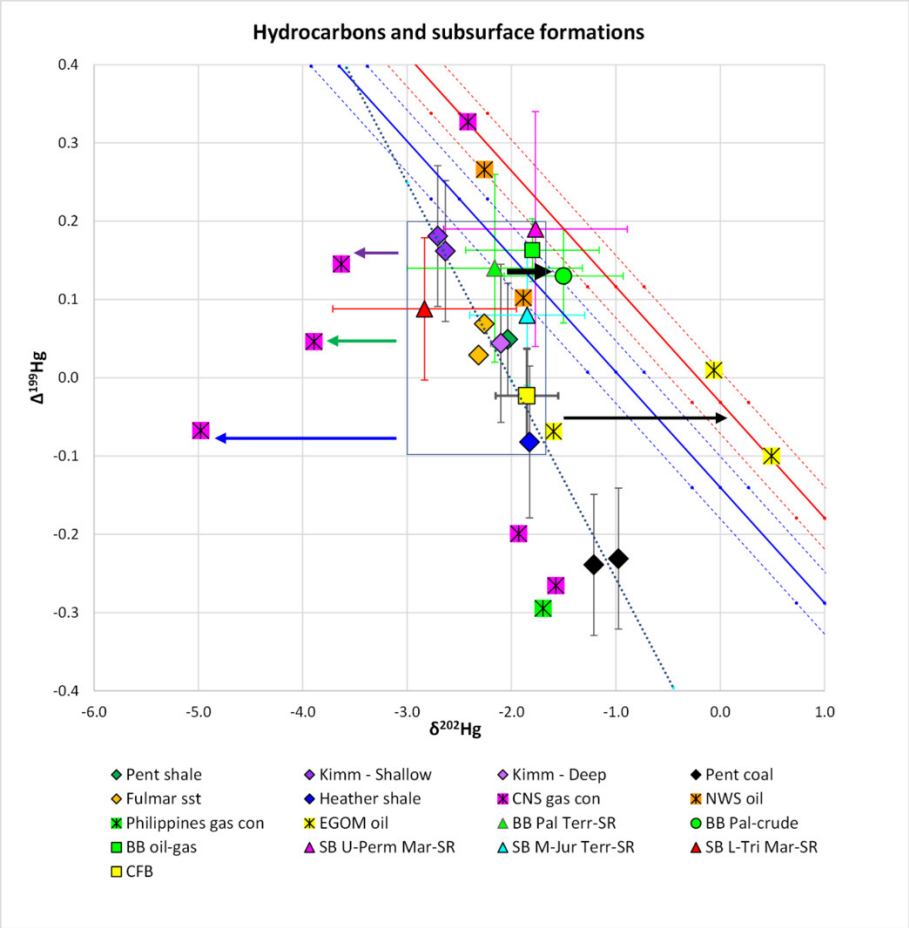

Figure 2. Isotopic compositions for a suite of source rocks (SR) and reservoir rocks from the CNS and China, including Paleogene terrestrial SR from Bohai Bay (BB), Upper Permian Marine SR from Sichuan Basin (SB), and Middle Jurassic terrestrial SR from Sichuan Basin (SB). Data for BB and SB SRs are from Zhou et al. (2023); BB oil-gas data are from Tang et al. (2019). The black rectangle outlines the area of clastic source rock shales (this study). Also plotted are a suite of hydrocarbons from the CNS, Eastern Gulf of Mexico (EGOM), the North West Shelf of Australia (NWS), and the Philippines (figure 1). The dotted black line is a "linear best fit" to the CNS source rock data. The short solid black arrow shows the shift in Hg isotopic composition associated with generation of gas and liquid hydrocarbons from Paleogene-age terrestrial source rock in Bohai Bay, from Zhou et al. (2023). The long solid black arrow is the inferred change in $\delta^{202}Hg$ for EGOM oils, as discussed in the text. The solid blue, green and purple arrows show expected volatilization trends of $^{198}Hg^0_{(g)}$ from source rock shales (solid-colored diamonds), as discussed in the text. Solid and dashed red and blue lines are the same as in figure 1. CFB refers to continental flood basalts from Yin et al. (2022). Error bars on source rocks represent ± 2σ analytical uncertainty.

middle Jurassic in the Sichuan Basin (SB, China). The dashed black line is a best fit to the CNS source rock data and is highlighted here because it shows that all of the potential source rocks in this part of the CNS likely contain an upper mantle Hg component, as indicated by the fact that the average CFB composition plots almost exactly on the CNS source rock trend.

3.1.3. Hydrocarbons

Mercury concentrations for liquid hydrocarbons are summarized in table S10 and includes samples from CNS, NWS, EGOM, and the Philippines. Samples from the EGOM are oils, while the remainder are gas condensate liquids. Concentrations of Hg are quite variable, and reflect similar ranges to that observed in source rocks, ranging from ~6 ppb to 307 ppb in samples from the CNS, to almost 880 ppb in a sample from the Philippines. Two of the condensate samples from the CNS are also enriched in Hg, with Hg concentrations of 137 and 307 ppb, respectively. It is reasonable, therefore, to infer that some of the hydrocarbons in the CNS likely derived their Hg from proximal Hg-enriched source rocks. Oils from the EGOM show a similar range of Hg enrichment also likely reflecting different Hg concentrations in their source rocks. The Hg enrichments observed in some of these hydrocarbon liquids are similar to ranges reported by Bryndzia et al. (2023) for Hg solubility in hydrocarbons.

Mass dependent fractionation of Hg isotopes in hydrocarbon liquids shown in figure 2 are somewhat unusual,

with a subset of hydrocarbon samples displaying significant depletions in MDF, with δ^{202}Hg ranging from −2.5‰ to −5‰, and Δ^{199}Hg ranging from −0.1 to 0.3‰ . Another subset of hydrocarbon samples mirrors an opposite trend, with significant enrichment in ^{202}Hg, with δ^{202}Hg = −2.5‰ to 0.5‰, plotting almost exactly on the MDF trend observed in Terlingua Hg ore minerals and OAE-2 sediments. The remaining three hydrocarbon samples show almost no MDF (δ^{202}Hg = −1.5 to −2‰), with Δ^{199}Hg = −0.3 to 0.1‰. Two of the EGOM oil samples plot on the Terlingua MDF-MIF and OAE-2 sediments trend.

3.2. Mass independent fractionation of Hg isotopes

Figure 3 shows the MIF of Hg isotopes for Hg deposits in table 1. Approximately 80% of the data (67 of 86 samples) plot within ± 0.1‰ of the origin, with many samples statistically indistinguishable from the MIF ranges of the upper mantle CFB Hg isotopic composition. Clear outliers on this plot are Hg ore minerals from Terlingua, and a few samples each from Almaden, Huancavelica, and Monte Amiata. Both cinnabar and hydrocarbons display strong positive and negative MIF. It is challenging to explain the distribution of the cinnabar data on this plot in terms of the broad groupings proposed by Moynier et al. (2021) and Yin et al. (2022), that distinguish domains for marine (positive MIF) and terrestrial reservoirs (negative MIF) for the source of Hg in various natural environments. On the Yin et al. (2022) MIF plot, almost all of the cinnabar ore minerals shown in the black circle in figure 3 would be considered to have a mantle source.

Figure 4 includes all of the source rocks and hydrocarbons discussed in figures 2 and 3, in addition to the bulk of the cinnabar data from figure 3 (black circle). Cinnabar ores from Terlingua and Huancavelica, and hydrocarbons, all show strong linear trends on the MIF Hg isotope plot. Both Terlingua and Huancavelica Hg ore minerals and associated hydrocarbons display positive Δ^{199}Hg fractionation relative to the bulk of the cinnabar ore data (black circle), and the isotopic trends for coals and euxinic sediments. Linear regressions defining trends for these three groups are shown in table 2. The solid black arrow in figure 4 indicates the MIF of Δ^{201}Hg isotopes due to hydrocarbon generation from the Bohai Bay Paleogene terrestrial source rock from Zhou et al. (2023). The magnitude of this MIF is ~0.5‰. Hydrocarbon generation occurs with negligible MIF of Δ^{199}Hg, and only minor depletion of Δ^{201}Hg. This also appears to be true for most of the source rocks in figure 4. Despite the apparently large analytical uncertainties associated with these data, hydrocarbons in general always appear to be depleted in Δ^{201}Hg relative to the general distribution of source rocks in figure 4. The only exceptions appear to be Upper Jurassic-age Kimmeridge shale and Lower Triassic marine source rock from the Sichuan Basin. It is also curious to note that the Bohai Bay Paleogene terrestrial source rock has pronounced positive Hg isotope MIF, and according to the designation of Moynier et al. (2021) and Yin et al. (2022), plots in the marine reservoir of Hg together with other marine source rocks. There are no published δ^{199}Hg or δ^{201}Hg data available for OAE-2 sediments from which to estimate and plot their Δ^{199}Hg or Δ^{201}Hg isotopic composition on figure 4. However, it is likely that they would closely track the linear trend observed for the Hg ore minerals in the Terlingua cinnabar ore deposits shown in figure 4. According to the classification of Yin et al. (2022), the Terlingua cinnabar deposits would be consistent with having a marine source for most of the Hg in their ore minerals (strong positive MIF). Similar inferences could be made for the Hg in the cinnabar ore minerals from the Huancavelica deposits in Peru, which also have samples with strong negative MIF, indicative of a terrestrial source of Hg (fig. 3).

4. DISCUSSION

4.1. Source rocks in the CNS graben

Source rocks from the CNS graben are the principal focus of this section since they provide the most representative example for the initial source of mantle-derived mercury being sequestered in organic-rich source rock sediments, and shows the impact of early diagenesis and subsequent thermal maturation of the organic matter on the isotopic composition of Hg isotopes in associated hydrocarbons.

There are potentially five source rocks in the CNS graben, including four shales and the Pentland coal. The Pentland coal and the Upper Jurassic-age Kimmeridge shale represent different environments of deposition (fig. 4), with the Pentland coal end-member forming in a near surface estuarine environment i.e., marine-terrestrial, while the shallow Kimmeridge shale end-member is clearly marine. Both the Pentland coal and Kimmeridge shale are enriched in Hg, with the shallow Kimmeridge samples containing 235 and 242 ppb Hg, respectively. The largest reservoir for Hg in the subsurface CNS formations is the Pentland coal, with Hg concentrations of 281 and 374 ppb, respectively (table S9). It is possible, therefore, that any of the CNS hydrocarbon samples in figure 2 could represent mixtures of hydrocarbons generated from either or both of these two Hg-enriched sediments (fig. 2). In TOC rich intervals, the environment of deposition is expected to be reducing and anoxic, or even euxinic, and favorable for sequestering Hg (Them et al., 2019).

This work shows that certain organic-rich source rocks are enriched in Hg, well above normal crustal abundances. However, many organic-rich source rocks contain much less Hg than the average crustal abundance of ~62.4 ppb Hg (Grasby et al., 2019). An excellent case in point are the shallow and deep Kimmeridge shales facies of the CNS graben (table S9). The shallow Kimmeridge black shale contains ~240 ppb Hg, while the deeper shale contains only ~46 ppb Hg. Black shales and marls in OAE-2 sediments from the lower Eagle Ford formation in SW Texas are similarly enriched, with Hg concentrations ranging from ~200–250 ppb in low-maturity organic-rich source rocks, and up to ~750 ppb from the producing sour black oil zone in the lower Eagle Ford formation, representing an enrichment of Hg in hydrocarbons by a factor of 3 (Bryndzia, 2023; Scaife et al., 2017).

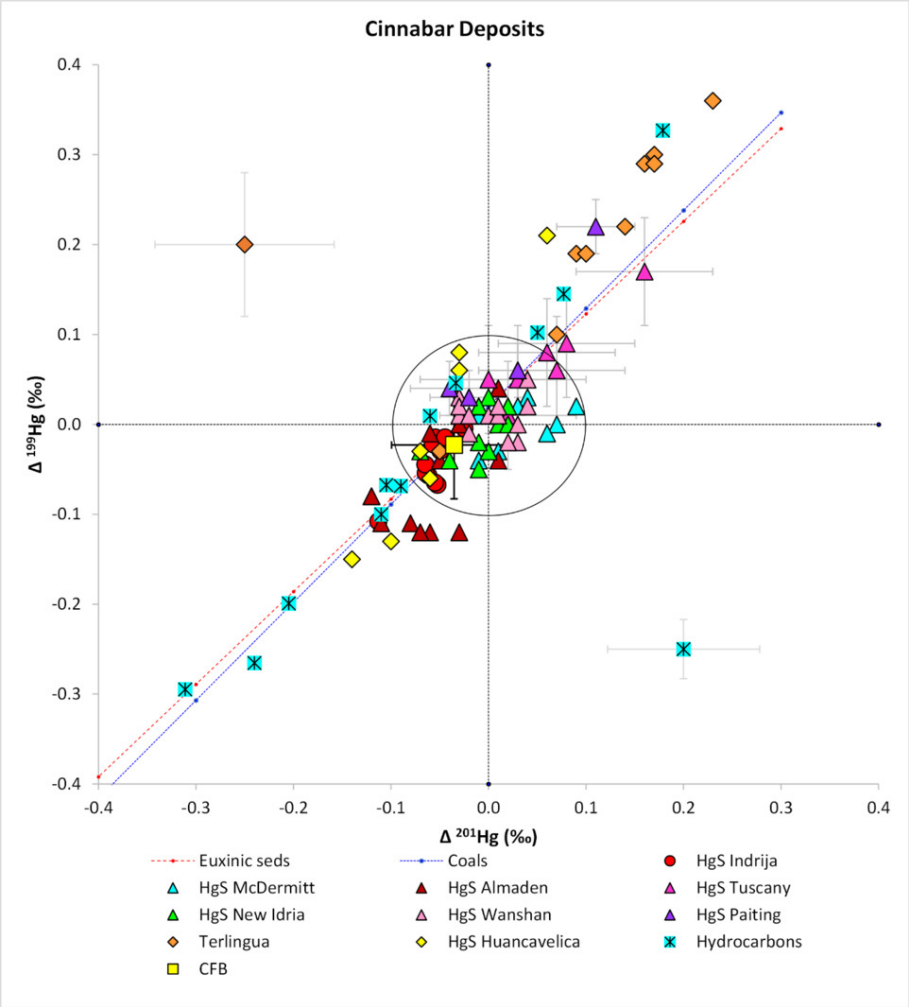

Figure 3. MIF plot of Hg isotope data for cinnabar deposits shown in table 1 and figures 1 and 2. Also plotted are the liquid hydrocarbons from figure 2. The circle represents ± 0.1 for both Δ^{201}Hg and Δ^{199}Hg. ~80% of the total set of cinnabar samples plot within the circle. Many samples are statistically indistinguishable from the MIF range of the mantle Hg isotopic composition as represented by the data for continental flood basalts (CFB). The dotted blue and red lines represent Hg isotopic compositions for euxinic sediments (organic-rich black shales) and coals from Zheng et al. (2018), and are included for reference. Average error bars on hydrocarbon and cinnabar symbols are ±2σ .

4.2. Hydrocarbons

Within analytical uncertainty, two of the CNS hydrocarbon samples in figure 2 plot close to the Pentland coal, while four of the CNS hydrocarbon samples appear to plot linearly displaced towards more depleted δ^{202}Hg isotopic compositions relative to their shale source rocks. The most striking aspect of the data in figure 2 is the very large MDF and MIF fractionation observed in the liquid hydrocarbons. The range of δ^{202}Hg in shales and coals ranges from ~ −1‰- −3‰, but in the liquid hydrocarbons it is almost three times larger, ranging from ~-5‰ to 0.5‰. Values of Δ^{199}Hg in source rocks ranges from ~ −0.25‰ to 0.2‰, while for liquid hydrocarbons the range is even larger, with Δ^{199}Hg = −0.1‰ to 0.3‰.

Figure 2 shows the results of liquid hydrocarbons generated under laboratory conditions from Paleogene terrestrial source rocks (Bohai Bay; Zhou et al., 2023). The Bohai Bay oil-gas data are from production samples from Tang et al. (2019), and are almost indistinguishable from the laboratory generated oils from the same source rocks (table S11). The short solid black arrow in figure 2 shows that there is very little Δ^{199}Hg MIF associated with the generation of hydrocarbons (liquids and gas), with a minor increase in the MDF, resulting in relative enrichment of ^{202}Hg in the generated hydrocarbons.

A similar inference may be made for the three oil samples from the EGOM, which show a similar enrichment in ^{202}Hg in hydrocarbon liquids generated from a source rock that is presumably proximal in origin to the dashed black source rock line in figure 2. The source rock for the EGOM oil samples is the upper Jurassic Haynesville Formation (Godo, 2017), an organic-rich black shale, age-equivalent to the Upper Kimmeridge source rock shale in the CNS. The data in figure 2 suggest that generation of liquid hydrocarbons from a source rock involves significant MDF, with both enrichment and depletion of ^{202}Hg, but with little MIF of

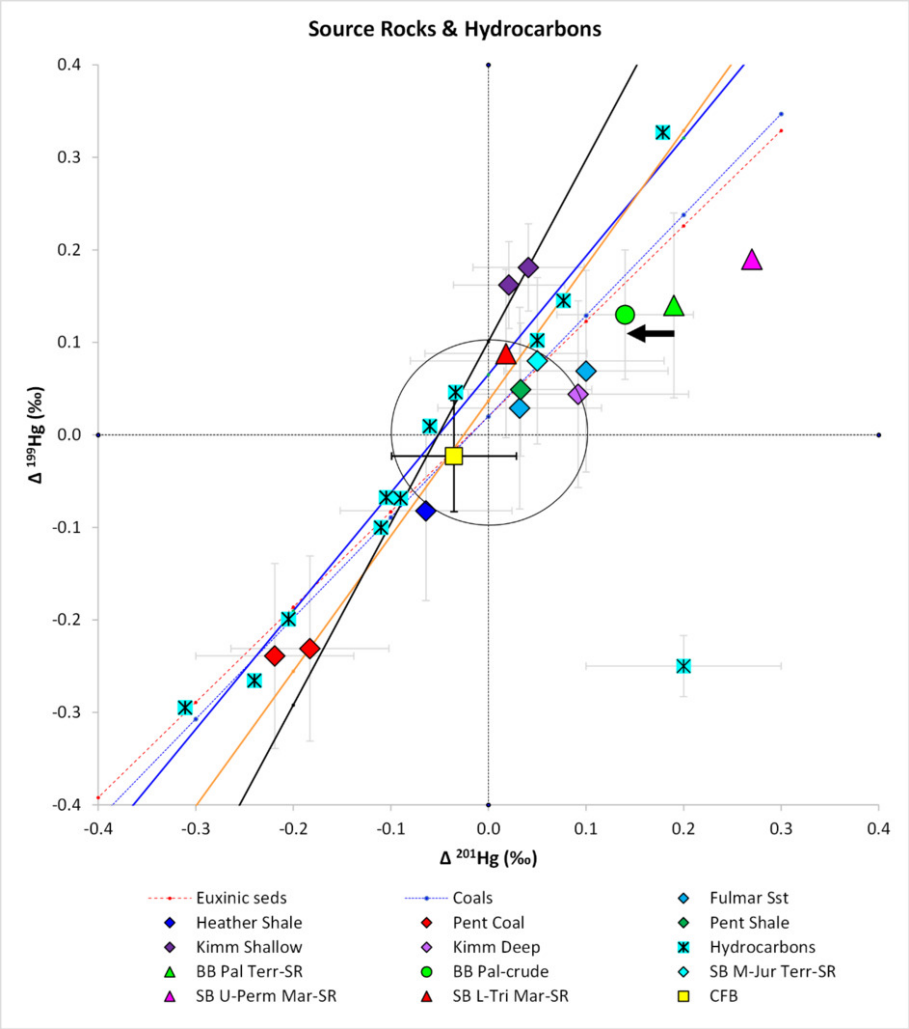

Figure 4. MIF plot of Hg isotope data that includes data for major cinnabar deposits (black circle), source rocks and hydrocarbons shown in figure 3. The three solid lines on this plot represent linear best fit models to the fractionation data from Terlingua (orange), Huancavelica (black), and ^{202}Hg depleted and enriched hydrocarbon liquids (blue) from table 2. The solid black arrow indicates MIF Hg isotope fractionation associated with hydrocarbon generation from Bohai Bay Paleogene terrestrial source rock (Zhou et al., 2023). The circle represents ± 0.1‰ for both Δ^{201}Hg and Δ^{199}Hg, as shown in figure 3. Average error bars on hydrocarbon and cinnabar symbols are ±2σ.

Table 2. Regression data for Δ^{199}Hg versus Δ^{201}Hg plots in figure 4 estimated using *IsoplotR* (*https://isoplotr.geo.utexas.edu/*)

Sample	Regression (± 2σ)	R^2 (n)
Terlingua	Δ^{199}Hg = 1.49 (± 0.69)*Δ^{201}Hg + 0.033 (± 0.10)	0.97 (9)
Huancavelica	Δ^{199}Hg = 2.05 (± 0.77)*Δ^{201}Hg + 0.11 (± 0.06)	0.94 (7)
Hydrocarbons	Δ^{199}Hg = 1.30 (± 0.24)*Δ^{201}Hg + 0.067 (± 0.04)	0.98 (11)

Δ^{199}Hg, as also observed by Chen et al. (2022) and Liu et al. (2022).

Experimental work by Indraswari et al. (2024) also generated hydrocarbon liquid from laboratory thermal maturation experiments on marine type II organic matter in Toarcian-age cores from the Lower Saxony Basin in Germany (Posidonienschiefer – Early Jurassic). A comparison of Hg data from three cores of increasing relative thermal maturity showed that Hg content in the mature/overmature sediments increased by over a factor of 2 compared to Hg in the immature cores. Hg enrichments in the highest maturity samples were found to be similar to the peak Hg anomaly in Siberian Traps (396 ppb; Wang et al., 2018), and Deccan Traps (415 ppb; Sial et al., 2013). However, the mechanism

of enrichment was not determined. They speculated that it was due to volatilization of Hg during heating. No Hg isotope data were included in the results of their study. One obvious explanation for the observed enrichment in Hg with thermal maturation is that $Hg^0_{(org)}$ was preferentially partitioned into a residual (liquid and/or bitumen) hydrocarbon phase.

Relative to the general Hg isotopic composition of hydrocarbon source rocks in figure 2 (black rectangle), two contrasting MDF Hg isotope trends are apparent in the hydrocarbon data. One trend clearly aligns with that observed in OAE-2 sediments and cinnabar ore minerals from Terlingua and Huancavelica (red and blue solid lines, respectively), and shows pronounced enrichment of ^{202}Hg. The other trend, typical of gas condensate liquids in the HP/HT CNS samples shows the opposite trend, with large depletions in ^{202}Hg, with $\delta^{202}Hg$ reaching ~−5‰.

One potential explanation for the observed depletion in ^{202}Hg in the gas condensate liquids could be attributed to volatilization of $^{198}Hg^0_{(g)}$ during thermal maturation of original kerogen in the shale source rock, as postulated by Indraswari et al. (2024). These samples are at present day reservoir temperatures ranging from ~171 to 182 °C. Gas condensates occur as a single phase, heavy molecular weight gas in subsurface reservoirs and it is reasonable to suggest that $Hg^0_{(g)}$, with its high vapor pressure, would preferentially fractionate the lighter mass ^{198}Hg isotope into a coexisting gas phase, as observed in the CNS gas condensate samples shown in figure 2, and confirmed experimentally by Estrade et al. (2009).

The solid-colored arrows in figure 2 show the expected volatilization trend of $Hg^0_{(g)}$ generated from CNS source rocks (colored diamonds) located within the black rectangle, and could explain the observed depletion in ^{202}Hg relative to its source rock composition. MDF due to volatilization of $^{198}Hg^0_{(g)}$ is significant, and apparently occurs without any MIF of $\Delta^{199}Hg$. The similarity in range of $\Delta^{199}Hg$ for both source rocks and hydrocarbons in figure 2 suggests that the $\Delta^{199}Hg$ isotopic composition of hydrocarbons is controlled by the $\Delta^{199}Hg$ isotopic composition of source rocks from which they were generated.

4.3. The role of hydrocarbons in cinnabar ore formation

A feature common to most cinnabar deposits is the ubiquitous presence of liquid hydrocarbons and bitumen, often giving rise to the term "hydrothermal petroleum" to describe the ubiquitous presence and role of hydrocarbons in the formation of most cinnabar deposits e.g., Yates et al. (1951), Yates and Thompson (1959), Bailey and Everhart (1964), Klemm and Neumann (1984), Krupp (1988), Noble and Vidal (1990), Saupe (1990), Peabody and Einaudi (1992), Spangenberg et al. (1999), Lavrič and Spangenberg (2003), Stetson et al. (2009), Wiederhold et al. (2013), Palero-Fernández et al. (2015), Schito et al. (2022), and Bryndzia (2023).

All of the giant cinnabar deposits shown in table 1 are associated with some form of hydrocarbon, either as liquid oil and/or bituminous residue after thermal degradation of original organic matter. In the case of the Terlingua deposits in SW Texas, Bryndzia (2023) showed that the Hg was likely remobilized both as $Hg^0_{(org)}$ and $Hg^0_{(aq)}$. Some of the purest and highest-grade cinnabar ores were formed as replacement deposits of fine grained smectitic clay minerals (Yates & Thompson, 1959), suggesting that Hg^{2+} was associated with smectitic clays formed as a result of hydrous alteration of siliceous volcanic debris, notably ash, glass and tuffaceous material. In the Terlingua deposits, thermal heating by intrusion of tabular igneous bodies generated liquid hydrocarbons that migrated into structurally favorable ore forming sites. Further analysis showed that both the age and cinnabar mineralization common in the California Coast Range deposits (New Idria and New Almaden), and Huancavelica (Peru) all likely formed in the same way, with Hg derived from Cenomanian-age organic-rich black shales, marls and interbedded tuffs i.e., OAE-2 sediments. All of these cinnabar deposits formed from sediments with similar isotopic compositions to those captured for the cinnabar deposits shown in figures 1, 2 and 3.

In addition to the ubiquitous presence and role that liquid hydrocarbons play in the formation of giant cinnabar deposits, the other critical component is H_2S. The primary control on cinnabar deposition is the ambient redox state. Significant concentrations of $Hg^0_{(org)}$ dissolved in liquid hydrocarbons are only possible in the presence of a relatively high fugacity of H_2S i.e., fH_2S. It is the oxidation of H_2S and Hg^0 that results in the deposition of cinnabar ores, generally brought about by mixing of migrating liquid hydrocarbons and associated formation brines, at shallow crustal levels with oxygenated meteoric waters (Bryndzia, 2023; Bryndzia et al., 2023; Krupp, 1988; Peabody & Einaudi, 1992).

4.4. Relationship between Hg isotopes in cinnabar ores and sediments/sedimentary rocks

4.4.1. Monte Amiata

Figure 5 shows the Hg isotopic composition of cinnabar from Terlingua and the Monte Amiata district in Tuscany (Italy), the third largest deposit of Hg in table 1. For such an historically significant Hg mining district surprisingly little is known about the source of Hg in the Monte Amiata deposits (D'Orazio et al., 2021; Klemm & Neumann, 1984; Rimondi et al., 2015; Schito et al., 2022). Descriptions of ore textures and mineralization by Klemm and Neumann (1984) are remarkably similar to those described for the Terlingua deposits by Yates and Thompson (1959), which Bryndzia (2023) showed were related to the organic-rich marls, claystones, black shales and altered tuffs forming part of the Cenomanian–Turonian OAE-2 sediments in the Terlingua mining district. Figure 5A shows that cinnabar ores from the Monte Amiata deposits plot between the Huancavelica and Terlingua ore trends. The Monte Amiata cinnabar ores are the only ones to confirm a strong genetic relationship to euxinic sediments, with a uniform slope of ~1 on the MIF plot in figure 5B.

Due to the emplacement of the Monte Amiata volcano and related intrusive igneous rocks at ~0.3 Ma, much of

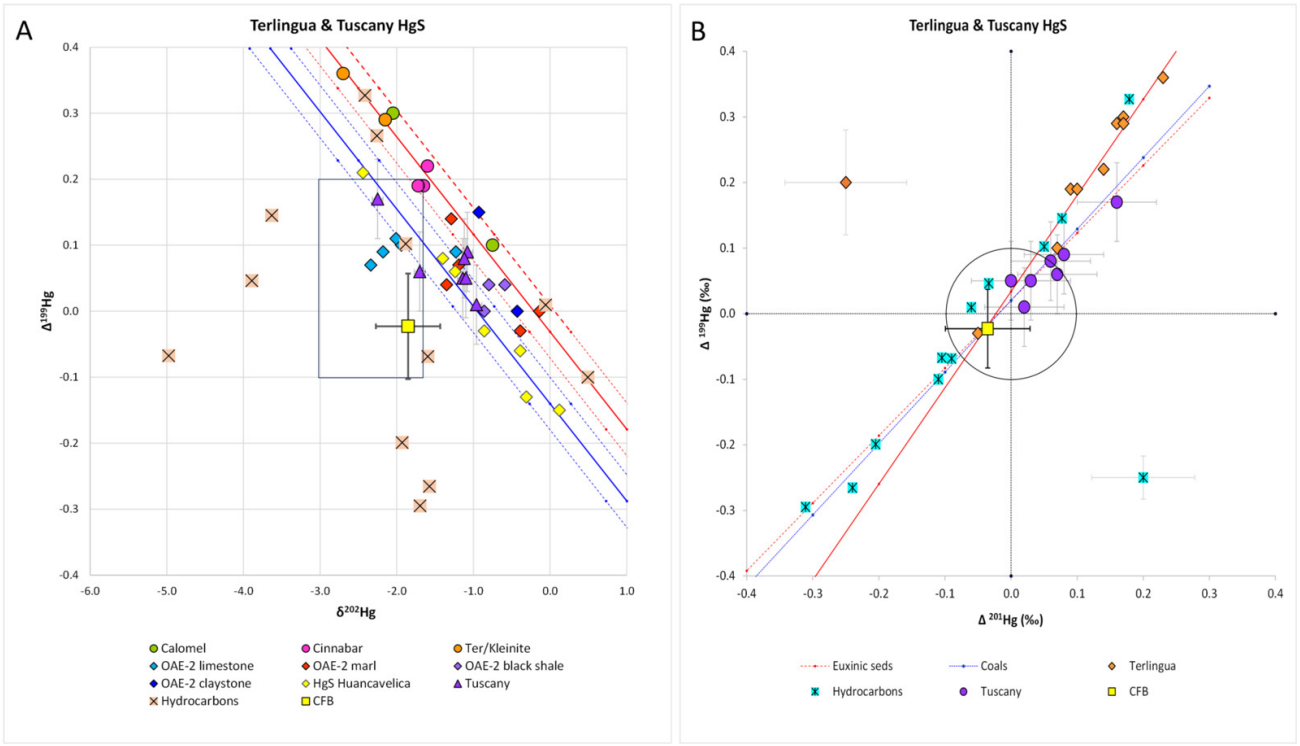

Figure 5. A) MDF-MIF Hg isotope data for Hg ore minerals from Terlingua (SW Texas; solid round symbols) and Monte Amiata (Tuscany). The black rectangle outlines the area of clastic source rock shales (fig. 2, this study). Also plotted are Hg isotope data from OAE-2 rocks, including limestone, marl, black shale and claystone from Rehkogelgraben, Austria (Yao et al., 2022). B) MIF-MIF plot of Hg isotopes for Hg ore minerals from Terlingua and Monte Amiata. The circle represents ± 0.1‰ for both Δ^{201}Hg and Δ^{199}Hg as shown in figure 3. Cinnabar ores from Tuscany are unique and plot along the MIF trend for coals and euxinic sediments, consistent with PZE in a marine environment of deposition.

the critical sedimentary stratigraphy in the Monte Amiata district is missing. OAE-2 sediments of Cenomanian–Turonian age are known to outcrop in the "Scaglia Toscana" formation in the Northern Apennines of northern Tuscany (D'Orazio et al., 2021). The rocks of this formation consist of shale, marl, marly limestone, calcilutite, calcarenite, radiolarite and calcareous-siliceous breccia. The black shales are also enriched in carbonaceous matter, containing 2–12 wt.% total organic carbon (TOC). Based on the hyper-enrichment in the elements Cd, Ag, Zn, Sb, Cu, Mo, V, Pb, and Tl in these sediments, D'Orazio et al. (2021) concluded that the black shales were deposited in a strongly anoxic and euxinic depositional environment, consistent with their MIF Hg isotopic composition in figure 5B. No Hg concentrations were reported for any of these sediments, which is surprising in view of the fact that they were so enriched in Zn (18,169, 12,581 ppm) and Cd (171, 94 ppm), and all are Group 12 elements.

4.4.2. Wanshan and Paiting

Figure 6 shows Hg isotopic data for the Cambrian-age Wanshan and Paiting cinnabar ores in SW China, including organic-rich, euxinic black shales from Maoshi and Zhijin (Yin et al., 2017; table S13), and black shales and tuffs from the Paiting Hg deposit (Ni et al., 2022; table S13). In figure 6A, many of the sediments plot in the source rock rectangle, while a significant number of samples also plot on the hydrocarbon-HgS mineralization trends for Terlingua and Huancavelica (red and blue lines, respectively). Cambrian black shales from both Maoshi and Zhijin are excellent source rocks, with very high levels of organic carbon and sulfur, and would have readily generated liquid hydrocarbons and H_2S from which the cinnabar ores would have been deposited. In figure 6A, Zhijin sediments in particular show significant enrichment in ^{202}Hg, approaching that observed in Wanshan cinnabar ore, while the Maoshi sediments show enriched δ^{202}Hg isotopic composition, with almost no variation in Δ^{199}Hg, consistent with loss of $^{198}Hg^0_{(g)}$. Tuffs and black shale from the Paiting Hg deposit plot between the Terlingua and Huancavelica cinnabar ore trends, with most of the tuffs plotting in a tight cluster with the Wanshan cinnabar ores.

In figure 6B the Zhijin sediments all lie in the domain of positive Hg isotope MIF where the dominant source of Hg is likely marine. Most of the Hg in the Wanshan cinnabar ores has a near zero MIF of Hg isotopes, consistent with an upper mantle isotopic signature. It does not appear that Hg in Wanshan and Paiting cinnabar ores was derived from either Maoshi or Zhijin black shales since there is almost no overlap in the Hg isotopes between these Cambrian-age sediments and cinnabar ores in figure 6B. The Hg isotopic signature of Wanshan cinnabar ores is very similar to those in basement tuffs and black shales from the Paiting de-

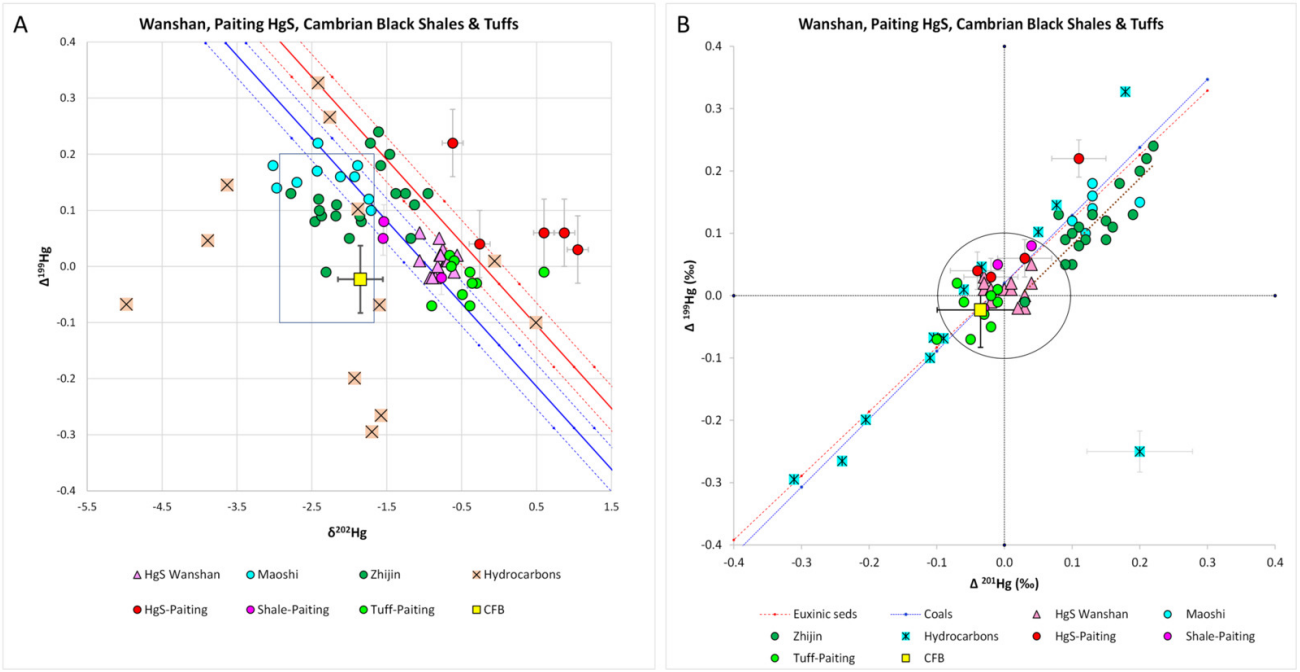

Figure 6. A) MDF-MIF Hg isotope data for HgS from Wanshan and Paiting, and Maoshi and Zhijin Cambrian black shales and tuffs from SW China (Yin et al., 2017). Most of the sediments plot in the source rock field (black rectangle). Maoshi black shales display enrichment in ^{202}Hg, with almost no variation in Δ^{199}Hg. Note that many of the Zhijin black shales plot along the Terlingua ore mineral trend (red line), consistent with OAE-2 black shales, claystone and marls. There is much better agreement for Wanshan cinnabar ores with tuffs and black shales from the Paiting Hg deposit than with sediments from Maoshi or Zhijin. B) MIF-MIF plot for Wanshan and Paiting HgS, Maoshi, Zhijin, and Paiting Cambrian black shales and tuffs. The circle represents ± 0.1‰ for both Δ^{201}Hg and Δ^{199}Hg as shown in figure 3. Most of the black shales plot below the trend for coals and euxinic sediments. Slope of dotted black line for the Zhijin black shales is 1.07, consistent with aqueous Hg^{2+} photo-reduction driven by dissolved organic matter with Δ^{199}Hg/Δ^{201}Hg ~1.02 (Bergquist & Blum, 2007). The excellent agreement between the Hg isotopic composition of Wanshan and Paiting cinnabar ores with black shales and tuffs from Paiting suggests that these were the main sources of Hg in the cinnabar ores.

posit, suggesting that these were the most likely progenitor sediments for the Wanshan and Paiting cinnabar ores. The slope of Δ^{199}Hg/Δ^{201}Hg for cinnabar from the Paiting Hg deposit ranges from 1.5 to 2, similar to cinnabar from Terlingua and Huancavelica. Ni et al. (2022) concluded that the Hg in the Paiting Hg deposit was mostly derived from Cambrian black shales. However, the Hg isotopic data in figure 6 strongly suggests that most of the Hg in Wanshan and Paiting cinnabar ores was derived from basement tuffs and related Cambrian black shales, and not the Maoshi or metalliferous Zhijin black shales.

4.4.3. Almaden, Indrija, and PTB sediments

The results of a similar exercise for cinnabar ores and Hg-enriched Permian–Triassic boundary (PTB) sediments are shown in figure 7 for the cinnabar ores from Almaden and Indrija. The PTB sediments include those identified as belonging to "trend II" by Sial et al. (2020; table S14), and include PTB samples from Indrijca (Slovenia), Rizvanusa (Croatia), Seres-101 (Southern Alps), and Hovea-3 (1980-94; SW Australia). Also plotted are Hg-enriched PTB sediments from Buchanan Lake (Canadian Arctic) from Grasby et al. (2017). In figure 7A, most of the PTB sediments plot within the source rock rectangle, including a few samples from Meishan. Most of the Meishan samples are enriched in ^{202}Hg and plot between the source rock rectangle and cinnabar ores of the same age. Several of the Meishan samples plot on the cinnabar ore trend relative to PTB samples. Note that all of the Buchanan Lake samples are enriched in ^{202}Hg relative to source rocks and other PTB sediments, including Meishan. By contrast, on the MIF Hg isotope plot in figure 7B, excellent agreement is observed between the PTB sediments from both sources, with almost complete overlap in the Hg isotopic compositions of cinnabar ores from both Almaden and Indrija. The latter observation strongly suggests that the dominant source of Hg in both the Almaden and Indrija cinnabar deposits is related to the PTB Hg-enriched sediments produced by the Siberian Traps LIP (STLIP).

According to Saupe (1990), the most probable source of mercury in the Almaden district is Ordovician black shale. However, there are also contemporaneous late Silurian–early Devonian black shales that form both hanging wall and footwall, respectively, to the Criadero Quartzite. Another Middle Black Shale unit occurs within the Criadero Quartzite, and all three shales are proximal to, or in direct contact with, the most Hg-rich syngenetic ore seams in Al-

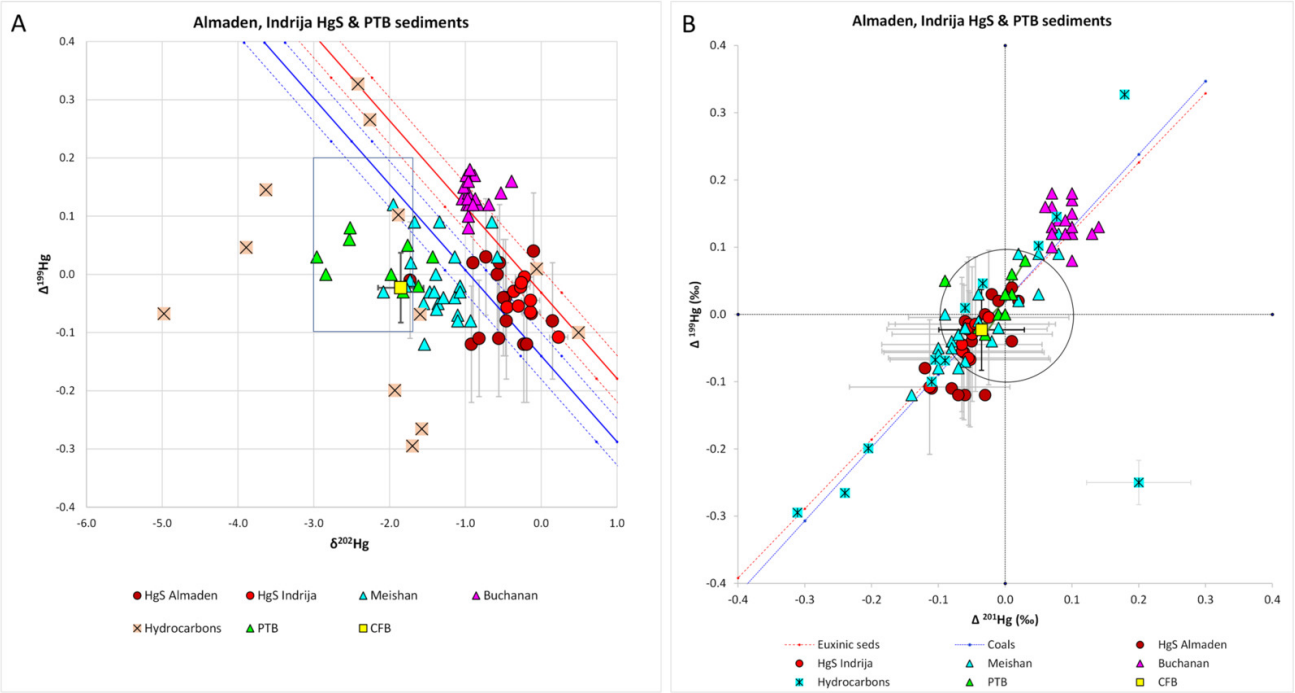

Figure 7. A) MDF-MIF Hg isotope data for HgS from Almaden (Spain) and Indrija (Slovenia), together with sediments from Meishan (China), Buchanan Lake (Canadian Arctic), and a sub-set of Permian–Triassic boundary (PTB) sediments from Sial et al. (2020). Most of the PTB sediments plot within the source rock rectangle, but most of the Meishan samples do not, lying between the source rock rectangle and cinnabar of the same age. Note that all of the Buchanan Lake samples are enriched in ^{202}Hg relative to source rocks and PTB sediments, including Meishan. B) MIF-MIF plot of Hg isotopes for HgS from Almaden and Indrija, together with PTB sediments from Meishan and Buchanan Lake (Grasby et al., 2017), and a sub-set of Permian–Triassic boundary (PTB) sediments from Sial et al. (2020). The circle represents ± 0.1‰ for both Δ^{201}Hg and Δ^{199}Hg as shown in figure 3. There is excellent agreement in MIF of Hg isotopes in PTB sediments from Meishan with HgS from both major cinnabar deposits, and the trend for euxinic sediments and coals. It is interesting to note that sediments from Buchanan Lake have strong positive MIF of Hg isotopes relative to HgS deposits of the same approximate age, while also appearing to cluster on the Terlingua ore minerals trend in A). Error bars on HgS samples represent ± 2σ analytical uncertainty and are the same for samples from both Almaden and Indrija.

maden (Palero-Fernández et al., 2015; their figure 7). There are no Hg isotope data available for any of these organic-rich black shales with which to correlate a potential LIP event or major source rock interval.

4.5. δ^{202}Hg isotope thermometry

Estrade et al. (2009) analyzed the Hg isotopic composition of $Hg^0_{(g)}$ during $Hg^0_{(liq)}$ evaporation experiments, both under equilibrium and dynamic mode fractionation conditions. For dynamic mode evaporation, they observed that the Hg isotopic composition of the condensed vapor phase was a strong function of temperature (Estrade et al., 2009; their fig. 3). The relationship they obtained is given by equation (1):

$$\delta^{202}Hg = 9.44 - 1.40 * 10^6/T^2\ (K) \qquad (1)$$

If Hg in the residual Hg pool preserves its isotopic composition when in equilibrium with cinnabar, using equation (1), it is possible to solve for the temperature at which cinnabar was in equilibrium with $^{198}Hg^0_{(g)}$. The results of this exercise for hydrocarbons are shown in table 3, and for cinnabar ores in table S16, respectively.

The inferred temperatures for the evaporation of Hg^0 observed in ^{202}Hg depleted gas condensate samples from the CNS are consistent with the experimental results of Estrade et al. (2009), and is taken as evidence in support of $^{198}Hg^0_{(g)}$ evaporation in organic-rich source rocks. If correct, the data in table 3 show that the evaporation of $^{198}Hg^0_{(g)}$ in source rocks generating δ^{202}Hg depleted hydrocarbon isotopic compositions is a relatively low temperature process. The evaporation of $^{198}Hg^0_{(g)}$ likely began early in the burial history of the source rock, coincident with the onset of the oil generation window at temperatures of ~65–80 °C (Horsfield & Rullkotter, 1994; Tissot & Welte, 1984). By contrast, the δ^{202}Hg isotopic composition of black oil samples in table 3 indicate much higher temperatures, similar to those inferred for cinnabar formation in table S16.

Assuming equilibrium of $^{198}Hg^0_{(g)}$ evaporation temperatures with $Hg^0_{(liq)}$ in the cinnabar forming reaction (eq 2; Bryndzia et al., 2023; Krupp, 1988) a model based on

$$Hg^0_{(liq)} + 0.5O_2 + H_2S \rightleftharpoons HgS + H_2O \qquad (2)$$

multiple linear regression of Δ^{199}Hg, δ^{202}Hg and temperature (eq 1), resulted in the model isotherms shown in figure

Table 3. Estimated temperatures of hydrocarbon formation from δ^{202}Hg isotopic composition[1]

Sample	Hydrocarbon type	δ^{202}Hg (‰)	Temp (°C)
CNS 09	gas condensate	-4.98	38.5
CNS 01	gas condensate	-3.89	50.9
CNS 07	gas condensate	-3.63	54.1
CNS 08	gas condensate	-2.42	70.5
NWS T-4	gas condensate	-2.26	72.8
NWS C-1	gas condensate	-1.88	78.5
EGOM V-1	black oil	-0.06	110.7
EGOM V-2	black oil	0.49	122.4

[1]This model assumes equilibrium between $^{198}Hg^0_{(g)}$ and $Hg^0_{(liq)}$ and evaporation temperatures, based on the experimental data from Estrade et al. (2009). Note the generally low temperatures associated with gas condensates relative to liquid black oils, which are similar to cinnabar formation temperatures shown in Table S16.

8. The upper limit of measured evaporation temperatures in Estrade et al. (2009) was 100 °C, so some extrapolation of the model to higher temperatures is required to accommodate all of the data. The model shows that the majority of cinnabar ores formed over a temperature range of ~80–140 °C, with samples from Almaden forming at the lowest temperature, and samples from Paiting indicating the highest formation temperatures of any major cinnabar deposit (fig. 8 and table S16).

A paucity of documented formation temperatures for cinnabar deposits in general makes any comparison with the data in figure 8 challenging. In some deposits the true cinnabar formation temperatures are much higher than shown in figure 8, as for example at Paiting, where Ni et al. (2022) report ore forming temperatures of 200–290 °C; and at Indrija, where Palinkaš et al. (2004) report cinnabar formation temperatures of 160–218 °C. For Monte Amiata, Rimondi et al. (2015) report fluid inclusion homogenization temperatures in calcite ranging from 80–130 °C and 70–120 °C respectively, from two different deposits, in good agreement with inferred formation temperatures shown in figure 8. The solid red and blue lines in figure 8 are the "best fit" linear trends observed for cinnabar ores from the Terlingua and Huancalevica deposits shown in figures 1 and 2, respectively. Both trends are almost exact overlays of the model isotherms. The obvious conclusion to be drawn from figure 8 is that MDF of Hg isotopes in cinnabar formation is a kinetic process i.e., mostly a function of temperature, and contrary to recent conclusions presented by Yang et al. (2025), is unlikely to be a reliable indicator of Hg provenance.

The cinnabar-derived temperatures in figure 8 are remarkably similar to the temperatures obtained from two black oil samples in table 3, and suggests that the cinnabar temperatures reflect both hydrocarbon generation and cinnabar formation related processes. This could explain the close similarity in the δ^{202}Hg isotopic composition between hydrocarbon liquids and cinnabar in figures 1 and 2. The onset of oil generation in a source rock is mostly a function of organic matter type, burial history, and kinetics of organic matter conversion (Horsfield & Rullkotter, 1994; Tissot & Welte, 1984). More importantly though, loss of a significant mass of $^{198}Hg^0_{(g)}$ to an extant gas phase would enrich any condensed liquid and residual organic matter in ^{202}Hg. This is a critical observation as it explains both the large depletions observed in the δ^{202}Hg isotopic compositions of gas condensates in the CNS data, as well as the enriched δ^{202}Hg isotopic composition observed in liquid hydrocarbons, cinnabar ores and OAE-2 sediments in figures 1 and 2. This is the fundamental characteristic of Hg isotopes common to all of the giant cinnabar deposits in table 1.

4.6. Δ^{199}Hg/Δ^{201}Hg ratios in hydrocarbons and cinnabar

Previous experimental and theoretical work has shown that slopes on Δ^{199}Hg–Δ^{201}Hg MIF plots may provide insights into the mechanism of MIF fractionations observed in nature (Estrade et al., 2009; Ghosh et al., 2013; Schauble, 2007; Wiederhold et al., 2010). Linear regression of MIF slopes i.e., Δ^{199}Hg/Δ^{201}Hg in figure 9 for Hg in Terlingua and Huancalevica cinnabar ores, and hydrocarbons were calculated using the errors-in-variables model (option 1) in the online version of *IsoplotR* software (*https://isoplotr.geo.utexas.edu*). Estimated 2σ in Δ^{199}Hg is ± 0.08 and ± 0.055 for cinnabar from Terlingua and Huancalevica, and ± 0.033 for hydrocarbons, respectively, while estimated uncertainties in Δ^{201}Hg are ± 0.09 and ± 0.05 for cinnabar from Terlingua and Huancalevica, and ± 0.078 for hydrocarbons, respectively.

The hydrocarbon Δ^{199}Hg/Δ^{201}Hg slope in figure 9 is 1.30 ± 0.69 (2σ). This is almost identical to that reported for photoreduction of CH_3Hg^+ to Hg^0 of 1.36 ± 0.03, attributed by Bergquist and Blum (2007) to the magnetic isotope effect (MIE) for MIF of Hg isotopes. It is possible that this is an inherited isotopic signature of photoreduction in the atmosphere or a shallow water setting i.e., photic zone, in the presence of dissolved organic matter, as proposed for Hg in sediments from Buchanan Lake by Grasby et al. (2017).

In the domain of negative MIF, the hydrocarbons plot almost exactly on the trends associated with euxinic sediments and coals. The slopes of the MIF isotopic fraction-

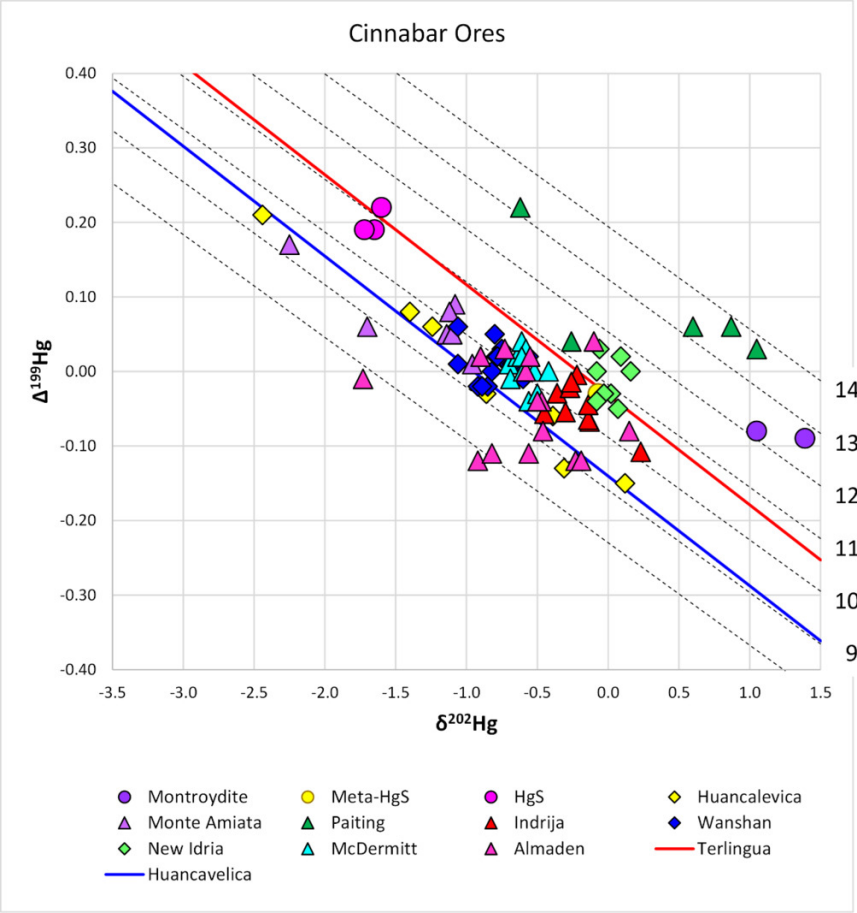

Figure 8. MDF-MIF plot of model isotherms from table S16, showing "relative" temperatures of cinnabar formation. According to this model, most cinnabar deposits formed over a temperature range of approximately 80–140 °C. The solid red and blue lines are the "best fit" linear trends observed for cinnabar from the Terlingua and Huancalevica deposits shown in figures 1 and 2, respectively. This figure shows that the dominant control on the MDF of Hg isotopes in cinnabar formation is temperature.

ation for euxinic sediments and coals are 1.09 and 1.03, respectively (Zheng et al., 2018). Photoreduction in this environment most likely represents the reduction of $Hg^{2+}_{(aq)}$ in the presence of organic matter, in a very reducing environment in which H_2S is also likely to be present i.e., photic zone euxinia (PZE). By contrast, in the domain of positive MIF (marine reservoir of Hg), hydrocarbons deviate significantly from the coal and euxinic MIF trends with $\Delta^{199}Hg/\Delta^{201}Hg$ ratios >1.0.

The MIF slopes observed in cinnabar from Terlingua and Huancavelica have $\Delta^{199}Hg/\ \Delta^{201}Hg$ slopes of ~1.49 ± 0.69 (2σ) and 2.05 ± 0.77 (2σ), respectively (table 2). Within analytical uncertainty these slopes are statistically the same as that reported by Wiederhold et al. (2010) for the equilibrium Hg isotope fractionation between dissolved Hg^{2+} and thiol-bound Hg, the dominant Hg-binding groups in natural organic matter, with a $\Delta^{199}Hg/\ \Delta^{201}Hg$ ratio of 1.54 ± 0.44 (2σ). Ghosh et al. (2013) confirmed these results, reporting a $\Delta^{199}Hg/\ \Delta^{201}Hg$ ratio of 1.59 ± 0.05 (2σ). Wiederhold et al. (2010) and Ghosh et al. (2013) both proposed that an MIF slope of $\Delta^{199}Hg/\ \Delta^{201}Hg$ of ~1.6 may be used to distinguish the nuclear volume effect (NVE) for MIF fractionation of Hg isotopes from the magnetic isotope effect (MIE) in natural samples and kinetic reactions.

4.7. Redox state and isotopic fractionation of Hg isotopes

The final stage in the development of a cinnabar deposit involves oxidation of $Hg^0_{(org,\ aq)}$ and H_2S to form cinnabar, as shown by equation (2). Oxidation of Hg^0 to Hg^{2+} is what defines the cinnabar ore deposition trend in the MDF-MIF Hg isotope plots shown in figures 1, and 2. These observations are also consistent with theoretical predictions that both mass dependent and nuclear volume fractionation mechanisms will enrich the heavy isotopes in the oxidized Hg species as compared to the reduced counterpart. More generally, nuclear-volume isotope fractionation will concentrate larger (heavier) nuclei in species where the electron density at the nucleus is small - due to lack of s-electrons e.g., oxidized Hg^{2+}–$[Xe]4f^{14}5d^{10}6s^0$ versus reduced Hg^0–$[Xe]4f^{14}5d^{10}6s^2$ (Schauble, 2007).

The increase in slope of hydrocarbons from the euxinic sediment and coal trends as indicated by the sediments from Buchanan Lake in figure 9 strongly suggests that the cause of the MIF in $\Delta^{199}Hg$ for Hg in both cinnabar and

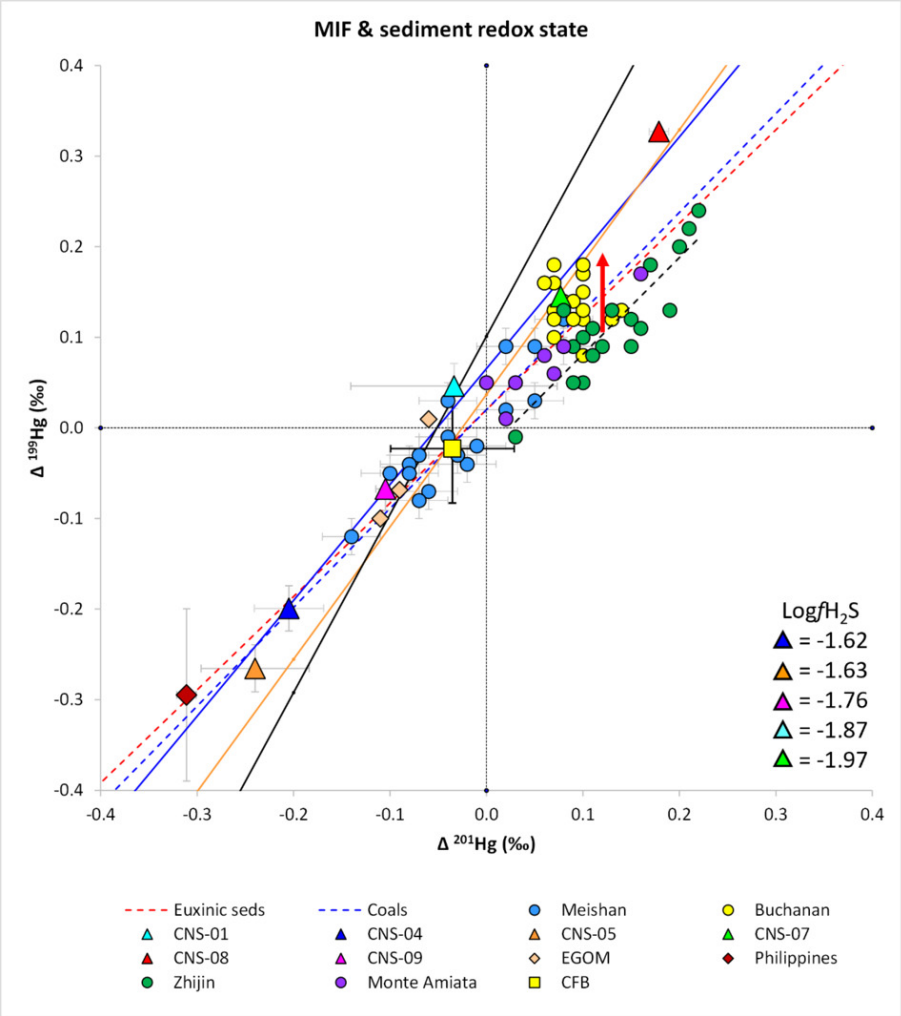

Figure 9. MIF Hg isotope plot for cinnabar from Monte Amiata (deposited under euxinic conditions; fig. 5), Hg-enriched sediments from Meishan, and euxinic sediments from Zhijin (fig. 6), and PTB sediments from Buchanan Lake (fig. 7). The solid black, orange, and blue lines are the linear best fit models to the MIF data for HgS from Huancalevica and Terlingua, and hydrocarbons, respectively (fig. 4, table 2). Error bars represent ± 2σ. The dashed black line represents a linear best fit to the euxinic black shales from Zhijin. The dashed blue and red lines represent Hg isotopic compositions for euxinic sediments (organic-rich black shales) and coals from Zheng et al. (2018), and are included for reference. The CNS hydrocarbons are color coded according to their LogfH_2S as shown in figure S3. The most oxidized CNS gas condensate sample (CNS-07) plots in the domain of positive MIF, together with the Hg-enriched PTB sediments from Buchanan Lake (Grasby et al., 2017). The bold red arrow indicates oxidation i.e., decrease in LogfH_2S, as discussed in the text.

in hydrocarbons may be controlled by the sediments themselves. Zheng et al. (2018) proposed that the negative Hg MIF isotope signature observed in organic-rich sediments in the geologic record, reflect reducing conditions in which H_2S is present in the absence of free oxygen i.e., PZE. He also suggested that in an oxic environment a positive MIF Hg isotope signature should be expected. Grasby et al. (2017; their fig. 3A) compared the Hg isotopic MIF in two different sets of PTB sediments, one from Buchanan Lake in the Canadian arctic, and the other from Meishan, in China. Both represent sediments from the PTB, but their environments of deposition were quite different, with Meishan representing a near-shore, shallow marine environment, while Buchanan Lake was representative of an open and deep marine environment. Comparison of Hg isotope systematics for these two different PTB sediments for MIF-MIF of Hg isotopes is shown in figure 9.

The essential differences in the Hg isotopes between the two PTB data sets is that Meishan sediments plot along the euxinic sediments and coal trend in figure 9, while the Buchanan Lake samples are all mostly enriched in Δ^{199}Hg relative to the Meishan sediments and the euxinic sediments and coal trends. This suggest that Hg in the Buchanan Lake sediments is more oxidized than in the Meishan sediments. Grasby et al. (2017) attributed the differences in Δ^{199}Hg MIF between these two sets of data to volcanic input in deep water marine environments for Buchanan Lake, while the near shore environment of deposition for Meishan have Δ^{199}Hg isotopic signatures of soil and/or biomass input, and that the deep marine signature is

overwhelmed in near shore locations due to Hg input from terrestrial sources. This shows that sediments forming in deep, open marine environments are likely to be more oxidized and contain more Hg^{2+}. By contrast, sediments forming in near-shore, shallow marine environments, although more likely to have a higher terrestrial Hg input, are also more reducing, with the dominant form of Hg likely to be Hg^0.

If the observed differences in slope on $\Delta^{199}Hg$ versus $\Delta^{201}Hg$ MIF plots are indeed controlled by the sediment redox state, then it is possible to test whether a relationship exists between fH_2S, and the isotopic composition of Hg in such a sediment. Estimation of fH_2S may be made using the equilibrium mineral-based model between iron chlorite, quartz, water and hydrocarbons, at any specified pressure and temperature. Model details and a work flow for its application is in Bryndzia and Villegas (2020), and will not be repeated here. The predicted fH_2S for the gas condensate reservoirs in the CNS is shown in figure S3. The fH_2S in figure S3 has been estimated at reservoir pressure and temperature, and is independent of the measured Hg isotopic composition. The fH_2S model for hydrocarbons from the CNS in figure S3 shows a well-defined linear trend for enrichment in $\Delta^{199}Hg$ as a result of decreasing fH_2S i.e., oxidation. More importantly, the most reduced and most oxidized samples behave in a consistent manner for both MDF and MIF of Hg isotopes in these gas condensate reservoirs. The single outlier in figure S3 has an fH_2S that is inconsistent with the rest of the gas condensate samples in this part of the CNS graben and is likely to have been derived from a deeper Triassic source.

Figure 9 shows the linear regression models for cinnabar ores from Terlingua, Monte Amiata, and Huancavelica, gas condensate reservoirs from the CNS, and Hg-enriched sediments from Zhijin, Meishan and Buchanan Lake (Grasby et al., 2017). The MIF slope for Meishan sediments (1.12 ± 0.32; 2σ), is similar to that of euxinic sediments from Zhijin (1.07) and euxinic sediments and coals (1.09 and 1.03, respectively). As indicated by the bold red arrow in figure 9, the data support the hypothesis that deviations in slopes of $\Delta^{199}Hg/\Delta^{201}Hg$ from the trends for euxinic sediments and coals do correlate with oxidation i.e., reduction in fH_2S. This is supported by the fact that in figure 9, the cluster of data from Buchanan Lake plots together with CNS-07, the most oxidized hydrocarbon sample from the CNS graben.

In general terms, the reservoir redox model supports the hypothesis that the slopes of $\Delta^{199}Hg$–$\Delta^{201}Hg$ MIF plots reflect relative differences in redox state of Hg-enriched sediments, particularly in the domain of positive Hg MIF. However, the present data does not permit conclusive demonstration of this hypothesis for different types of sediment. This should be the focus of further research, and recent progress addressing this issue has been made by Frieling et al. (2023). The important observation demonstrated by figure S3 is that small variations in $\Delta^{199}Hg$ MIF of Hg isotopes are to be expected as a result of natural variations in redox state for sediments deposited in different environments, such as open deep-marine versus shallow nearshore, as proposed by Grasby et al. (2017).

5. CONCLUSIONS

It is the ubiquitous generation of hydrocarbons from Hg- and organic-rich sediments that results in a dramatic increase in Hg enrichment in reduced hydrothermal fluids i.e., oils and brine, termed by numerous researchers as "hydrothermal petroleum". $Hg^0_{(org)}$ has relatively high solubility in hydrocarbon liquids as does $Hg^0_{(aq)}$ in brines, and as recently demonstrated for the Terlingua Hg deposits in SW Texas, these are the principal ore-forming fluids responsible for the deposition of the giant cinnabar deposits in table 1.

MIF mercury isotope data for most cinnabar ores closely resembles the Hg isotopic composition of CFBs, and provides compelling evidence that Hg in most cinnabar deposits, globally distributed throughout geologic time, all share an original upper mantle origin for their Hg. MDF of mercury isotopes in cinnabar show that Hg was sourced from Hg-enriched sediments, some of which record globally significant LIP events and are associated with hydrocarbons generated from organic-rich source rocks and sediments, such as the OAE-2, NAIP, and ST LIPs, for example.

Hg isotopes confirm an upper mantle source for Hg in a suite of hydrocarbon source rocks in the CNS graben. The upper Jurassic Pentland coal and Kimmeridge shale both received their Hg endowment from the same Jurassic volcanic event that also generated conditions favorable for producing the organic-rich Kimmeridge black shale source rock. This is the first time that a mantle source has been shown to be the potential source of Hg in a suite of hydrocarbon source rocks in a major hydrocarbon producing province.

Significant depletions in ^{202}Hg are observed in HP/HT gas condensates from reservoirs in the CNS graben, consistent with partitioning of $^{198}Hg^0_{(g)}$ into a hydrocarbon gas phase during early diagenesis of organic-rich source rock shales. The volatilization of $^{198}Hg^0_{(g)}$ is accompanied by early loss of labile H_2S, and is independent of MIF of Hg isotopes.

Cinnabar in all deposits is unusually enriched in ^{202}Hg relative to CFB, its nominal upper mantle source. There are two principal causes for the observed enrichments in ^{202}Hg. One is due to significant loss of $^{198}Hg^0_{(g)}$ resulting in a ^{202}Hg enriched residual Hg pool, from which ^{202}Hg-enriched liquid hydrocarbons and $Hg^0_{(org)}$ were later generated. The other is caused by oxidation of coexisting $Hg^0_{(org)}$, $Hg^0_{(aq)}$, and H_2S at the site of cinnabar deposition. This is the reason why the MDF trend of $\delta^{202}Hg$ in the Hg ore minerals in the Terlingua and Monte Amiata deposits is similar to the $\delta^{202}Hg$ isotopic enrichment trend observed in OAE-2 sediments from the type locality in Rehkogelgraben, Austria.

The $\Delta^{199}Hg/\Delta^{201}Hg$ slope for hydrocarbons is 1.30 ± 0.24 (2σ) and is almost identical to that reported for photoreduction due to the MIE. The $\Delta^{199}Hg/\Delta^{201}Hg$ slopes for cinnabar from Terlingua and Huancalevica are consistent with previously published experimental studies suggesting that MIF of Hg isotopes in cinnabar was due to the NVE.

The Almaden Hg deposits in Spain represent the largest enrichment of Hg on Earth. The age of the host sediments

for these deposits is Silurian–Devonian, yet the unambiguous Hg isotope signature for these deposits (and the Indrija Hg deposits in Slovenia), are the PTB sediments associated with the Permian–Triassic Siberian Traps LIP, confirmed by the Pb isotope ages of cinnabar mineralization.

In the domain of positive MIF, deviations in Δ^{199}Hg from linear trends for coals and euxinic sediments with Δ^{199}Hg /Δ^{201}Hg slopes of ~1, is due to variable redox conditions in the sediments, controlled by the relative proportion of reduced and organic-rich material in which the dominant form of Hg is Hg^0, and oxidized tuffaceous sediments in which the dominant form of Hg is Hg^{2+}. This hypothesis is supported by estimates of fH_2S in CNS gas condensate reservoirs in which Δ^{199}Hg is strongly correlated to fH_2S.

ACKNOWLEDGMENTS

LTB is grateful to Shell International Exploration & Production Inc. for approving Release of Technical Data included in this paper, and to Associate Professor Ilia Rodushkin, Laboratory Manager, ALS Scandinavia AB, for providing details on Hg isotope analyses on hydrocarbons and subsurface rock samples used in this study.

This paper benefitted from reviews by Dr. Paul G. Spry, two anonymous reviewers, and the editorial guidance of Editor Dr. Mark Brandon and Associate Editor Dr. Timothy W. Lyons.

FUNDING

No external funding was associated with the research and writing of this paper

DATA AND SUPPLEMENTARY INFORMATION

https://doi.org/10.5061/dryad.2547d7x5j

AUTHOR CONTRIBUTIONS

LTB designed and performed the research, analyzed the data, prepared the figures, wrote the paper and is wholly accountable for its content.

COMPETING INTEREST STATEMENT

The author declares no conflict of interest.

Editor: Mark T. Brandon, Associate Editor: Timothy W. Lyons

Submitted: August 07, 2023 EST. Accepted: November 05, 2025 EST. Published: January 20, 2026 EST.

REFERENCES

Bailey, E. H., & Everhart, D. L. (1964). *Geology and quicksilver deposits of the New Almaden District, Santa Clara County, California* (Professional Paper No. 360). U.S. Geological Survey. https://doi.org/10.5962/bhl.title.45586

Bergman, S. C., Eldrett, J. S., & Minisini, D. (2021). Phanerozoic Large Igneous Province, Petroleum System, and Source Rock Links. *Geophysical Monograph Series*, 191–228. https://doi.org/10.1002/9781119507444.ch9

Bergquist, B. A. (2017). Mercury, volcanism, and mass extinctions. *Proceedings of the National Academy of Sciences*, *114*(33), 8675–8677. https://doi.org/10.1073/pnas.1709070114

Bergquist, B. A., & Blum, J. D. (2007). Mass-Dependent and -Independent Fractionation of Hg Isotopes by Photoreduction in Aquatic Systems. *Science*, *318*(5849), 417–420. https://doi.org/10.1126/science.1148050

Bryndzia, L. T. (2023). Elucidating the Role of Hydrocarbons in Cinnabar (HgS) Ore Formation: A Model for Hg Mineralization in the Terlingua Mining District, Big Bend National Park, SW Texas. *Economic Geology*, *118*(8), 1881–1897. https://doi.org/10.5382/econgeo.5022

Bryndzia, L. T., Burgess, J. M., & Bourdet, J. (2023). Predicting the Solubility of Mercury in Hydrocarbons. *SPE Journal*, *28*(02), 859–875. https://doi.org/10.2118/212271-pa

Bryndzia, L. T., & Villegas, E. I. (2020). Predicting the Concentration of Hydrogen Sulfide in Hydrocarbon-Bearing Clastic Reservoirs: Introducing the Iron-Chlorite-Pyrite-Hydrogen Sulfide Model. *SPE Journal*, *25*(06), 3186–3199. https://doi.org/10.2118/201190-pa

Chen, D., Ren, D., Deng, C., Tian, Z., & Yin, R. (2022). Mercury loss and isotope fractionation during high-pressure and high-temperature processing of sediments: Implication for the behaviors of mercury during metamorphism. *Geochimica et Cosmochimica Acta*, *334*, 231–240. https://doi.org/10.1016/j.gca.2022.08.010

D'Orazio, M., Biagioni, C., & Mantovani, D. (2021). Late Cretaceous black shales from the Tuscan Sedimentary Succession (northern Tuscany, Italy): geochemistry and ore mineralogy. *Italian Journal of Geosciences*, *140*(2), 221–236. https://doi.org/10.3301/ijg.2020.30

Eldrett, J. S., Ma, C., Bergman, S. C., Lutz, B., Gregory, F. J., Dodsworth, P., Phipps, M., Hardas, P., Minisini, D., Ozkan, A., Ramezani, J., Bowring, S. A., Kamo, S. L., Ferguson, K., Macaulay, C., & Kelly, A. E. (2015). An astronomically calibrated stratigraphy of the Cenomanian, Turonian and earliest Coniacian from the Cretaceous Western Interior Seaway, USA: Implications for global chronostratigraphy. *Cretaceous Research*, *56*, 316–344. https://doi.org/10.1016/j.cretres.2015.04.010

Estrade, N., Carignan, J., Sonke, J. E., & Donard, O. F. X. (2009). Mercury isotope fractionation during liquid-vapor evaporation experiments. *Geochimica et Cosmochimica Acta*, *73*(10), 2693–2711. https://doi.org/10.1016/j.gca.2009.01.024

Frieling, J., Mather, T. A., März, C., Jenkyns, H. C., Hennekam, R., Reichart, G. J., Slomp, C. P., & van Helmond, N. A. G. M. (2023). Effects of redox variability and early diagenesis on marine sedimentary Hg records. *Geochimica et Cosmochimica Acta*, *351*, 78–95. https://doi.org/10.1016/j.gca.2023.04.015

Ghosh, S., Schauble, E. A., Lacrampe Couloume, G., Blum, J. D., & Bergquist, B. A. (2013). Estimation of nuclear volume dependent fractionation of mercury isotopes in equilibrium liquid-vapor evaporation experiments. *Chemical Geology*, *336*, 5–12. https://doi.org/10.1016/j.chemgeo.2012.01.008

Godo, T. (2017). The Appomattox Field: Norphlet Aeolian Sand Dune Reservoirs in the Deep-Water Gulf of Mexico. In *Giant Fields of the Decade 2000-2010* (pp. 29–54). https://doi.org/10.1306/13572000m1133680

Grasby, S. E., Shen, W., Yin, R., Gleason, J. D., Blum, J. D., Lepak, R. F., Hurley, J. P., & Beauchamp, B. (2017). Isotopic signatures of mercury contamination in latest Permian oceans. *Geology*, *45*(1), 55–58. https://doi.org/10.1130/g38487.1

Grasby, S. E., Them, T. R., II, Chen, Z., Yin, R., & Ardakani, O. H. (2019). Mercury as a proxy for volcanic emissions in the geologic record. *Earth-Science Reviews*, *196*, 102880. https://doi.org/10.1016/j.earscirev.2019.102880

Gray, J. E., Pribil, M. J., & Higueras, P. L. (2013). Mercury isotope fractionation during ore retorting in the Almadén mining district, Spain. *Chemical Geology*, *357*, 150–157. https://doi.org/10.1016/j.chemgeo.2013.08.036

Horsfield, B., & Rullkotter, J. (1994). Diagenesis, catagenesis, and metagenesis of organic matter. *The Petroleum System – From Source to Trap*, *60*, 189–199. https://doi.org/10.1306/M60585C10

Indraswari, A. O., Frieling, J., Mather, T. A., Dickson, A. J., Jenkyns, H. C., & Idiz, E. (2024). Investigating the Behavior of Sedimentary Mercury (Hg) During Burial-Related Thermal Maturation. *Geochemistry, Geophysics, Geosystems*, *25*(6). https://doi.org/10.1029/2024gc011555

Jenkyns, H. C. (2010). Geochemistry of oceanic anoxic events. *Geochemistry, Geophysics, Geosystems*, *11*(3). https://doi.org/10.1029/2009gc002788

Jones, M. T., Percival, L. M. E., Stokke, E. W., Frieling, J., Mather, T. A., Riber, L., Schubert, B. A., Schultz, B., Tegner, C., Planke, S., & Svensen, H. H. (2019). Mercury anomalies across the Palaeocene-Eocene Thermal Maximum. *Climate of the Past*, *15*(1), 217–236. https://doi.org/10.5194/cp-15-217-2019

Klemm, D. D., & Neumann, N. (1984). Ore-controlling factors in the Hg-Sb province of southern Tuscany, Italy. In A. Wauschkuhn, C. Kluth, & R. A. Zimmermann (Eds.), *Syngenesis and Epigenesis in the Formation of Mineral Deposits*. Springer. https://doi.org/10.1007/978-3-642-70074-3_44

Krupp, R. (1988). Physicochemical aspects of mercury metallogenesis. *Chemical Geology*, *69*(3–4), 345–356. https://doi.org/10.1016/0009-2541(88)90045-9

Lavrič, J. V., & Spangenberg, J. E. (2003). Stable isotope (C, O, S) systematics of the mercury mineralization at Idrija, Slovenia: constraints on fluid source and alteration processes. *Mineralium Deposita*, *38*(7), 886–899. https://doi.org/10.1007/s00126-003-0377-9

Liu, Z., Tian, H., Yin, R., Chen, D., & Gai, H. (2022). Mercury loss and isotope fractionation during thermal maturation of organic-rich mudrocks. *Chemical Geology*, *612*, 121144. https://doi.org/10.1016/j.chemgeo.2022.121144

Moynier, F., Jackson, M. G., Zhang, K., Cai, H., Halldórsson, S. A., Pik, R., Day, J. M. D., & Chen, J. (2021). The Mercury Isotopic Composition of Earth's Mantle and the Use of Mass Independently Fractionated Hg to Test for Recycled Crust. *Geophysical Research Letters*, *48*(17). https://doi.org/10.1029/2021gl094301

Ni, X., Yang, R., Yuan, W., Wang, X., Chen, J., Zhang, G., Li, D., Du, L., Gao, L., Luo, C., Zheng, L., & Xu, H. (2022). New insight into the source of metals in Hg deposits at the southwestern margin of the Yangtze Platform, China: Evidence from mercury stable isotope compositions. *Ore Geology Reviews*, *149*, 105089. https://doi.org/10.1016/j.oregeorev.2022.105089

Noble, D. C., & Vidal, C. C. E. (1990). Association of silver with mercury, arsenic, antimony, and carbonaceous material at the Huancavelica District, Peru. *Economic Geology*, *85*(7), 1645–1650. https://doi.org/10.2113/gsecongeo.85.7.1645

Palero-Fernández, F. J., Martin-Izard, A., Zarzalejos Prieto, M., & Mansilla-Plaza, L. (2015). Geological context and plumbotectonic evolution of the giant Almadén Mercury Deposit. *Ore Geology Reviews*, *64*, 71–88. https://doi.org/10.1016/j.oregeorev.2014.06.013

Palinkaš, L., Strmić, S., Spangenberg, J., Prochaska, W., & Herlec, U. (2004). Ore-forming fluids in the Grübler orebody, Idrija mercury deposit, Slovenia. *Swiss Bulletin of Mineralogy and Petrology*, *84*(1), 173–188.

Peabody, C. E., & Einaudi, M. T. (1992). Origin of petroleum and mercury in the Culver-Baer cinnabar deposit, Mayacmas District, California. *Economic Geology*, *87*(4), 1078–1103. https://doi.org/10.2113/gsecongeo.87.4.1078

Percival, L. M. E., Bergquist, B. A., Mather, T. A., & Sanei, H. (2021). Sedimentary Mercury Enrichments as a Tracer of Large Igneous Province Volcanism. *Geophysical Monograph Series*, 247–262. https://doi.org/10.1002/9781119507444.ch11

Rimondi, V., Chiarantini, L., Lattanzi, P., Benvenuti, M., Beutel, M., Venturi, S., Colica, A., Costagliola, P., Gabbani, G., Gray, J. E., Pandeli, E., Pattelli, G., Paolieri, M., & Ruggieri, G. (2015). Metallogeny, exploitation and environmental impact of the Mt. Amiata mercury ore district (Southern Tuscany, Italy). *Italian Journal of Geosciences*, *134*(2), 323–336. https://doi.org/10.3301/IJG.2015.02

Saupe, F. (1990). Geology of the Almadén mercury deposit, province of Ciudad Real, Spain. *Economic Geology*, *85*(3), 482–510. https://doi.org/10.2113/gsecongeo.85.3.482

Scaife, J. D., Ruhl, M., Dickson, A. J., Mather, T. A., Jenkyns, H. C., Percival, L. M. E., Hesselbo, S. P., Cartwright, J., Eldrett, J. S., Bergman, S. C., & Minisini, D. (2017). Sedimentary Mercury Enrichments as a Marker for Submarine Large Igneous Province Volcanism? Evidence From the Mid-Cenomanian Event and Oceanic Anoxic Event 2 (Late Cretaceous). *Geochemistry, Geophysics, Geosystems*, *18*(12), 4253–4275. https://doi.org/10.1002/2017gc007153

Schauble, E. A. (2007). Role of nuclear volume in driving equilibrium stable isotope fractionation of mercury, thallium, and other very heavy elements. *Geochimica et Cosmochimica Acta*, *71*(9), 2170–2189. https://doi.org/10.1016/j.gca.2007.02.004

Schito, A., Muirhead, D., Bowden, S., & Parnell, J. (2022). Hydrothermal generation of hydrocarbons in basement rocks, Southern Tuscany. *Italian Journal of Geosciences*, *141*(2), 231–244. https://doi.org/10.3301/ijg.2022.10

Schlanger, S., & Jenkyns, H. (1976). Cretaceous Oceanic Anoxic Events: Causes and Consequences. *Geologie En Mijnbouw*, *55*(3–4), 179–184.

Sial, A. N., Chen, J., Lacerda, L. D., Frei, R., Tewari, V. C., Pandit, M. K., Gaucher, C., Ferreira, V. P., Cirilli, S., Peralta, S., Korte, C., Barbosa, J. A., & Pereira, N. S. (2016). Mercury enrichment and Hg isotopes in Cretaceous–Paleogene boundary successions: Links to volcanism and palaeoenvironmental impacts. *Cretaceous Research*, *66*, 60–81. https://doi.org/10.1016/j.cretres.2016.05.006

Sial, A. N., Chen, J., Lacerda, L. D., Korte, C., Spangenberg, J. E., Silva-Tamayo, J. C., Gaucher, C., Ferreira, V. P., Barbosa, J. A., Pereira, N. S., & Benigno, A. P. (2020). Globally enhanced Hg deposition and Hg isotopes in sections straddling the Permian-Triassic boundary: Link to volcanism. *Palaeogeography, Palaeoclimatology, Palaeoecology*, *540*, 109537. https://doi.org/10.1016/j.palaeo.2019.109537

Sial, A. N., Lacerda, L. D., Ferreira, V. P., Frei, R., Marquillas, R. A., Barbosa, J. A., Gaucher, C., Windmöller, C. C., & Pereira, N. S. (2013). Mercury as a proxy for volcanic activity during extreme environmental turnover: The Cretaceous-Paleogene transition. *Palaeogeography, Palaeoclimatology, Palaeoecology*, *387*, 153–164. https://doi.org/10.1016/j.palaeo.2013.07.019

Spangenberg, J. E., Hunziker, J. C., Meisser, N., & Herlec, U. (1999). *Compound specific isotope analysis of the organic minerals hatchettite and idrialite in geodes, coal, and mineral deposits* (pp. 275–278). Balkema.

Stetson, S. J., Gray, J. E., Wanty, R. B., & Macalady, D. L. (2009). Isotopic Variability of Mercury in Ore, Mine-Waste Calcine, and Leachates of Mine-Waste Calcine from Areas Mined for Mercury. *Environmental Science & Technology*, *43*(19), 7331–7336. https://doi.org/10.1021/es9006993

Tang, S., Zhou, Y., Yao, X., Feng, X., Li, Z., Wu, G., & Guangyou, Z. (2019). The mercury isotope signatures of coalbed gas and oil-type gas: Implications for the origins of the gases. *Applied Geochemistry*, *109*, 104415. https://doi.org/10.1016/j.apgeochem.2019.104415

Them, T. R., II, Jagoe, C. H., Caruthers, A. H., Gill, B. C., Grasby, S. E., Gröcke, D. R., Yin, R., & Owens, J. D. (2019). Terrestrial sources as the primary delivery mechanism of mercury to the oceans across the Toarcian Oceanic Anoxic Event (Early Jurassic). *Earth and Planetary Science Letters*, *507*, 62–72. https://doi.org/10.1016/j.epsl.2018.11.029

Thibodeau, A. M., Ritterbush, K., Yager, J. A., West, A. J., Ibarra, Y., Bottjer, D. J., Berelson, W. M., Bergquist, B. A., & Corsetti, F. A. (2016). Mercury anomalies and the timing of biotic recovery following the end-Triassic mass extinction. *Nature Communications*, *7*(1). https://doi.org/10.1038/ncomms11147

Tissot, B. P., & Welte, D. H. (1984). Sedimentary Processes and the Accumulation of Organic Matter. In *Petroleum Formation and Occurrence* (pp. 55–62). https://doi.org/10.1007/978-3-642-87813-8_5

Wang, X., Cawood, P. A., Zhao, H., Zhao, L., Grasby, S. E., Chen, Z.-Q., Wignall, P. B., Lv, Z., & Han, C. (2018). Mercury anomalies across the end Permian mass extinction in South China from shallow and deep water depositional environments. *Earth and Planetary Science Letters*, *496*, 159–167. https://doi.org/10.1016/j.epsl.2018.05.044

Wiederhold, J. G., Cramer, C. J., Daniel, K., Infante, I., Bourdon, B., & Kretzschmar, R. (2010). Equilibrium Mercury Isotope Fractionation between Dissolved Hg(II) Species and Thiol-Bound Hg. *Environmental Science & Technology*, *44*(11), 4191–4197. https://doi.org/10.1021/es100205t

Wiederhold, J. G., Smith, R. S., Siebner, H., Jew, A. D., Brown, G. E., Jr., Bourdon, B., & Kretzschmar, R. (2013). Mercury Isotope Signatures as Tracers for Hg Cycling at the New Idria Hg Mine. *Environmental Science & Technology*, *47*(12), 6137–6145. https://doi.org/10.1021/es305245z

Yang, B., Yang, C., Tian, Z., Deng, C., Lehmann, B., & Yin, R. (2025). Unique mercury isotopic signature of mercury-bearing hydrothermal systems in South China and its geological and environmental implications. *Geology*, *53*(3), 238–242. https://doi.org/10.1130/g52619.1

Yao, H., Chen, X., Wagreich, M., Grasby, S. E., Liu, S.-A., Yin, R., Tostevin, R., Lv, Y., Gu, X., Liu, X., & Wang, C. (2022). Isotopic evidence for changes in the mercury and zinc cycles during Oceanic Anoxic Event 2 in the northwestern Tethys, Austria. *Global and Planetary Change*, *215*, 103881. https://doi.org/10.1016/j.gloplacha.2022.103881

Yates, R. G., Kent, D. F., & Concha, J. F. (1951). *Geology of the Huancavelica quicksilver district, Peru* (USGS Bulletin 975-A). U.S. Geological Survey.

Yates, R. G., & Thompson, G. A. (1959). *Geology and quicksilver deposits of the Terlingua district, Texas* (USGS Professional Paper No. 312). U.S. Geological Survey. https://doi.org/10.3133/pp312

Yin, R., Chen, D., Pan, X., Deng, C., Chen, L., Song, X., Yu, S., Zhu, C., Wei, X., Xu, Y., Feng, X., Blum, J. D., & Lehmann, B. (2022). Mantle Hg isotopic heterogeneity and evidence of oceanic Hg recycling into the mantle. *Nature Communications*, *13*(1). https://doi.org/10.1038/s41467-022-28577-1

Yin, R., Xu, L., Lehmann, B., Lepak, R. F., Hurley, J. P., Mao, J., Feng, X., & Hu, R. (2017). Anomalous mercury enrichment in Early Cambrian black shales of South China: Mercury isotopes indicate a seawater source. *Chemical Geology*, *467*, 159–167. https://doi.org/10.1016/j.chemgeo.2017.08.010

Zheng, W., Gilleaudeau, G. J., Kah, L. C., & Anbar, A. D. (2018). Mercury isotope signatures record photic zone euxinia in the Mesoproterozoic ocean. *Proceedings of the National Academy of Sciences*, *115*(42), 10594–10599. https://doi.org/10.1073/pnas.1721733115

Zhou, Y., Tang, S., Algeo, T. J., Shen, J., & Li, Y. (2023). Mercury isotope variation during organic matter maturation to petroleum. *Chemical Geology*, *618*, 121298. https://doi.org/10.1016/j.chemgeo.2022.121298

SUPPLEMENTARY MATERIALS

Supplementary material

Download: https://ajsonline.org/article/147533-from-source-rock-to-cinnabar-how-the-giant-mercury-deposits-in-earth-s-crust-formed/attachment/322282.zip